Research Square

Preprints are preliminary reports that have not undergone peer review.
They should not be considered conclusive, used to inform clinical practice,
or referenced by the media as validated information.

# The Impact of Drying Method on the Hierarchical Structure and Porosity of Cellulose Beads Regenerated from Superbase Ionic Liquids

**Matti Leskinen**
University of Helsinki
**Marianna Kemell**
University of Helsinki
**Ilkka Kilpeläinen**
University of Helsinki
**Vladimir Aseyev**
vladimir.aseyev@helsinki.fi

University of Helsinki

**Research Article**

**Keywords:** Cellulose, Superbase Ionic Liquid, Drying, Porosity, Morphology, Particles

**Posted Date:** November 12th, 2026

**DOI:** https://doi.org/10.21203/rs.3.rs-10981199/v1

**License:** This work is licensed under a Creative Commons Attribution 4.0 International License.
Read Full License

**Additional Declarations:** No competing interests reported.

# The Impact of Drying Method on the Hierarchical Structure and Porosity of Cellulose Beads Regenerated from Superbase Ionic Liquids

Matti Leskinen,*[1] Marianna Kemell,[1] Ilkka Kilpeläinen,[1] Vladimir Aseyev*[1]

[1]*University of Helsinki, Department of Chemistry, P.O. Box 55, FI-00014 UH, Helsinki, Finland*

*Corresponding authors:

Vladimir Aseyev

vladimir.aseyev@helsinki.fi

https://orcid.org/0000-0002-3739-8089

Matti Leskinen

matti.l.leskinen@helsinki.fi

https://orcid.org/0000-0002-5126-5020

Non-corresponding authors:

Marianna Kemell

marianna.kemell@helsinki.fi

https://orcid.org/0000-0002-3583-2064

Ilkka Kilpeläinen

ilkka.kilpelainen@helsinki.fi

https://orcid.org/0000-0001-8582-2174

## Abstract

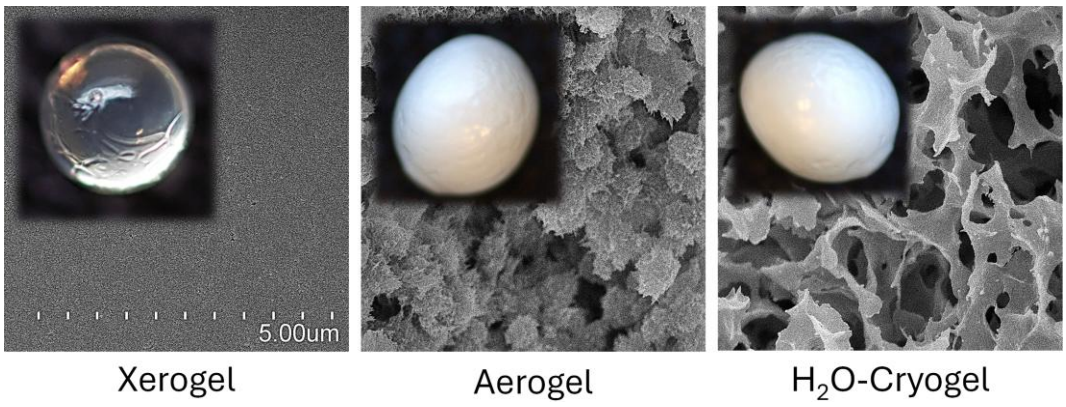
Superbase ionic liquids (SBILs), such as 1,5-diazabicyclo[4.3.0]non-5-enium acetate, [DBNH][OAc], dissolve cellulose under mild dissolution conditions and low dope viscosities, enabling shape-controlled regeneration. We prepared regenerated cellulose beads from cellulose/[DBNH][OAc]/DMSO solution via drop-wise addition into water, and subsequently dried the obtained hydrogels by ambient evaporation (xerogel), freeze-drying from $H_2O$ or tert-butanol (cryogels), or supercritical $CO_2$ (aerogel). It was shown that dring methods, that avoid capillary forces and ice templating, best preserve the hydrogel nanostructure formed during regeneration. Accordingly, aerogels exhibited high specific surface area (SSA 450 $m^2\ g^{-1}$) and mesopore volume (1.98 $cm^3\ g^{-1}$), exceeding those values for tBuOH cryogels (123 $m^2\ g^{-1}$; 0.45 $cm^3\ g^{-1}$) and for $H_2O$ cryogels (29 $m^2\ g^{-1}$; 0.06 $cm^3\ g^{-1}$) by factors of ~4 and ~16 in SSA, respectively, while xerogels were essentially non-porous (0.04 $m^2\ g^{-1}$) and practically transparent. SEM revealed regeneration-

derived spherical substructures in aerogels that progressively consolidated through cryogels and vanished in xerogels. SAXS identified characteristic length scales near 30 and 63 nm and Porod exponents consistent with increasingly smooth interfaces upon consolidation, confirming systematic shifts in morphology with the drying severity. These results link regeneration pathway and drying route to hierarchical morphology in SBIL-derived cellulose, providing design rules for tailoring porosity for adsorption and related applications.

**Keywords**

*Cellulose, Superbase Ionic Liquid, Drying, Porosity, Morphology, Particles*

## Graphical abstract



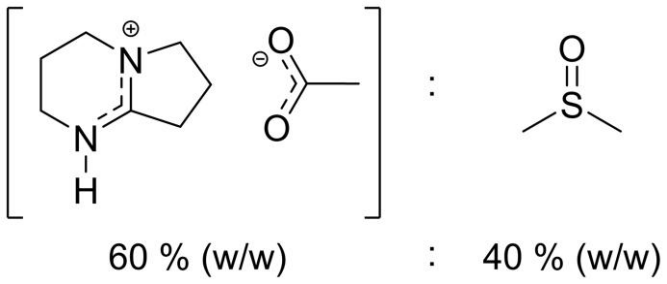

# Introduction

The growing urgency to develop environmentally sustainable materials has led to great interest in the potential of cellulose as a renewable source of raw material and cellulose processing as a viable alternative to petroleum-based processes. Particularly cellulose dissolution and regeneration have been the subjects of much research activity, where a great number of solvents have been tested for their cellulose dissolving capacity. The common solvents studied for these purposes include aqueous inorganic bases such as NaOH and LiOH and their mixtures with urea/thiourea (Roy et al. 2003, Cai et al. 2008 Gavillon & Budtova 2008, Luo & Zhang 2009, Luo & Zhang 2010, Lu et al. 2011, Isobe et al. 2012, Trygg et al. 2013, Yildir et al. 2013, Demilecamps et al. 2014, Yu et al. 2014, Lin et al. 2017, Qiao et al. 2020), inorganic salt hydrates (Ganesan et al. 2016, Pircher et al. 2016, Liao et al. 2019), inorganic salts mixed with solvents such as LiCl/DMA and TBAF/DMSO (Carrick et al. 2014, Pircher et al. 2016, Li et al. 2020), and organic salt hydrates such as NMMO·$H_2O$ (Biganska et al. 2002, Biganska & Navard 2005, Gavillon & Budtova 2008, Biganska & Navard 2009, Beaumont et al. 2016, Hauru et al. 2016, Pircher et al. 2016, Beaumont et al. 2017, Ilyin et al. 2018, Nishiyama et al. 2019). While these solvent systems have a proven efficiency and clear benefits in being direct or at least semi-direct cellulose solvents, and hence enabling homogeneous liquid state processing, each carry a certain set of process limitations such as high viscosity, poor environmental stability and recyclability, or hazardous process conditions. Driven by shortcomings such as these, development of new alternative cellulose solvents has continued.

Ionic liquids (ILs), organic salts with a commonly used upper limit on melting point of 100 °C, are a solvent group from which multiple effective cellulose solvents have been identified. These

compounds, while observed already in the early-to-mid 20th century, have seen renewed research interest through the 21st century after their efficacy to cellulose processing was recognized. (Swalotski et al. 2002) Of the various ILs, the family of imidazolium-based ILs, including compounds such as [emim][OAc], [amim]Cl and [bmim]Cl (Aaltonen & Jauhiainen 2009, Deng et al. 2009, Sescousse et al. 2011, Song et al. 2013, Östlund et al. 2013, Suzuki et al. 2014, Ding et al. 2015, Buchtová & Budtova 2016, Hauru et al. 2016, Mi et al. 2016, Pircher et al. 2016, Imagawa et al. 2017, Johns et al. 2017, Omura et al. 2017, Rajeev & Basavaraj 2019, Lin & Jana 2021), has seen much use in cellulose processing studies.

Nevertheless, more recently identified IL families, such as the superbase ionic liquids (SBILs) based on a superbase conjugate acid cation, show much potential with easy processability and improved dissolving capacity. (King et al. 2011, Parviainen et al. 2013, Sixta et al. 2015, Hauru et al. 2016, Kuzmina et al. 2017, Sturm et al. 2023, Leskinen et al. 2024a) Among others, mixtures of a SBIL 1,5-diazabicyclo[4.3.0]non-5-enium acetate ([DBNH][OAc]) with DMSO show several benefits. Cellulose dopes in neat [DBNH][OAc] have a lower viscosity and can be operated at lower temperatures compared to a common direct cellulose solvent NMMO·$H_2O$ (Sixta et al. 2015; Hauru et al. 2016). Mixing the IL with a neutral molecular solvent such as DMSO creates an organic electrolyte solution OES (Gericke et al. 2011, Clough 2017), which in case of [DBNH][OAc]/DMSO (60:40 w/w) (see Scheme 1), increases the cellulose dissolving capacity and lowers the melting point of the mixture below RT for improved handling (Parviainen et al. 2013, Holding 2016).




**Scheme 1** Components of the organic electrolyte solution OES, 1,5-diazabicyclo[4.3.0]non-5-enium acetate and dimethyl sulfoxide [DBNH][OAc]/DMSO (40 wt-% DMSO). The 60:40 w/w composition was used throughout the current study.

The preparation of spherical or bead-like particles from dissolved cellulosic base materials via antisolvent regeneration has been demonstrated previously in the scientific literature. The polymeric base has varied from cellulose derivates such as cellulose acetate (Motozato & Hirayama 1984, Bai & Li 2006, Sandig et al. 2015) to composites of cellulose and inorganic compounds such as $Fe_2O_3$ and $CoFe_2O_4$ nanoparticles (Luo & Zhang 2009, Luo & Zhang 2010, Yu et al. 2014) to pure cellulose dissolved in a variety of solvents. These solvents used to prepare beads from chemically unmodified cellulose can generally be divided into four groups: (i) aqueous inorganic bases such as NaOH & KOH and their urea/thiourea mixtures (Trygg et al. 2013, Yildir et al. 2013, Lin et al. 2017, Qiao et al. 2020), (ii) inorganic salt electrolytes such as LiCl/DMAc (Carrick et al. 2013, Carrick et al. 2014, Li et al. 2020), (iii) heterocyclic amine oxide hydrates such as NMMO·$H_2O$ (Beaumont et al. 2017) and (iv) ionic liquids and their electrolytes such as [bmim]Cl, [bmim]Cl/DMF, [bmim][OAc], [DBNH][$CO_2$Et] or [DBNH][OAc]/DMSO. (Omura et al. 2017, Druel et al. 2018, Zeng et al. 2020, Leskinen et al. 2024b) While several different methods have been applied to imparting the round, bead-like shape onto a cellulose particle, one of the most straightforward ones is to introduce a solution of cellulose into an excess cellulose antisolvent in a dropwise manner.

While the difficulty of achieving straightforward and controllable cellulose dissolution and regeneration has been the focus of much research during the past few decades, it is the eventual drying step which can have the most wide-ranging effect on the properties of the final cellulose material. Despite progress with IL- and SBIL-based cellulose regeneration, the interplay between regeneration-derived mesostructure (spinodal substructures) and subsequent drying route across aerogel/cryogel/xerogel outcomes remains insufficiently quantified, particularly in SBIL/OES

systems. Here we consider the three methods for drying such antisolvent-soaked regenerated cellulose as ambient drying, freeze-drying and supercritical drying. Each of these methods relies on the removal of the antisolvent from the cellulose material, principally differing from each other by the necessity of a solvent-exchange and the nature of the phase transition the antisolvent undergoes during the final drying process. The dry materials obtained from these different drying methods (supercritical-drying, freeze-drying and ambient-drying) can be generally categorized as aerogels, cryogels and xerogels respectively.

Small and wide angle X-ray scattering was used to study mesostructure (SAXS) and the crystalline and amorphous morphology (WAXS) of cellulose, which are useful characteristics in evaluating the impact and effectiveness of various chemical and physical treatments. SAXS is used to study nanoscale cellulose structures such as fibre bundles and matrix cross-sections. WAXS is often used to determine the proportion of crystalline regions relative to the amorphous regions (i.e. the crystallinity index, CI) and the morphology (I, II, III, IV) of the cellulose crystallites. Each of the common cellulosic morphologies such as Cellulose I, Cellulose II and amorphous cellulose have their characteristic signals in the WAXS-diffractogram. There are several methods used for determination of cellulose degree of crystallinity based on WAXS data, with the most widely used methods being based on peak height (Segal), amorphous subtraction (Ruland-Vonk), deconvolution (Rietveld) and Debye calculations. (Thygesen et al. 2005, Park et al. 2010).

This work integrates nitrogen sorption (BET/BJH), SEM, and SAXS to link regeneration-derived mesostructures to final porosity and interfacial morphology. We report a systematic analysis of how a drying route - ambient drying (xerogel), freeze-drying from water or tert-butanol (cryogels), and supercritical $CO_2$ drying (aerogel) - minimizes capillary stress and ice templating, and controls the hierarchical structure of cellulose beads regenerated from an organic electrolyte solution consisting of DMSO and a superbase ionic liquid [DBNH][OAc]. We relate Porod exponents and characteristic length scales to drying route and the degree of consolidation.

# Experimental

## Materials

Microcrystalline cellulose (MCC, powder 20 μm, Sigma-Aldrich, catalogue number 310697), 1,5-diazabicyclo[4.3.0]non-5-ene (DBN, Fluorochem, catalogue 044323), glacial acetic acid (Fisher Scientific, catalogue A/0400/PB15), and dimethyl sulfoxide (DMSO, Fisher Scientific, catalogue D/4121/PB15) were used without further purification. Distilled water was used in all experiments (Aquator A4S).

## Preparation of samples

### *Preparation of [DBNH][OAc]/DMSO*

[DBNH][OAc]/DMSO was prepared by mixing equimolar amounts of DBN and glacial acetic acid together followed by addition of DMSO. The resulting OES, [DBNH][OAc]/DMSO (40 wt-% DMSO has low viscosity due to DMSO and melting point below the room temperature (RT) making the handling of the OES easier in further process steps. Following earlier reports (Parviainen et al. 2013; Holding 2016), the OES composition of 40 wt-% DMSO and 60 wt-% IL was found to be suitable for cellulose dissolution, and offered improved handling over the neat IL, due to below-RT melting point and lowered viscosity. During storage, the OES was placed under argon in a desiccator. To prepare wet, i.e. water-containing OES mixtures, OES was weighed in a 20 ml vial, and the appropriate amount of distilled water was added to obtain ca. 10 ml of liquid of the wanted mixing ratio (90:10 to 10:90 w/w water:OES).

### *MCC dissolution*

To prepare a total of 10 g of 5 wt-% solution of cellulose, 0.5 g of MCC was added slowly to 9.5 g of OES in a 20 ml glass vial under stirring at RT. Mixing of the components results in cloudy, heterogeneous cellulose suspension, which was placed under inert gas (Ar). The suspension was heated to 60 °C under continued stirring until the liquid appeared optically transparent. Afterwards, the acquired dope was left to cool to RT without stirring. More Ar was applied after cooling, the cap was sealed well, and the dope was stored as is for further use. Viscosity measurements of OES and dope can be found in our earlier publication. (Leskinen et al. 2024a)

### *Regeneration of cellulose beads*

The cellulose dope was regenerated into cellulose hydrogel beads by dropwise extrusion through a needle (0.8 mm diameter) into a vial holding 600 ml of distilled water (10 cm dropping height). Gentle stirring was employed assisting in gradual and smooth interdiffusion of water and OES.

Regenerated beads were washed five times with distilled water by decanting and replacing the volume of water in the bath with an equivalent amount every 15 min. Finally, the procured hydrogel beads were left to soak in water for further 24 h, after which they were washed once more before being stored in excess distilled water. A detailed description of the bead regeneration process and measurements of bead dimensions can be found in our earlier publication. (Leskinen et al. 2024b)

### *Drying cellulose beads*

The hydrogel beads were dried in one of several ways to obtain distinct cellulose morphologies: ambient-drying for xerogels, freeze-drying (from $H_2O$ or tBuOH) for cryogels or supercritical-drying (from $CO_2$) for aerogels. Preparing xerogel beads via ambient-drying consists of spreading the hydrogel beads on a petri-dish or other flat container, draining out excess $H_2O$ from around the beads and letting the remaining $H_2O$ evaporate in a RT laboratory fume hood. The forming xerogel beads were usually fully dry after 24 h, but larger batches required 48 h for drying. The drying process can be expedited by faster removal of atmospheric moisture from around the beads, which is achieved by spacing the beads wide apart and placing the container below a local exhaust ventilation. This way total drying time can be reduced to 1 h, especially for small sample amounts.

The aqueous freeze-drying ($H_2O$) process consists of freezing the wet beads with liquid nitrogen and placing them in a freeze-dryer (Labconco FreeZone 2.5 Plus) maintained at -40 °C and under high vacuum. The tBuOH freeze-drying process consists of a solvent exchange into tBuOH (see below) and transfer of the beads into a round-bottom flask, which is placed into an ethanol bath (-20 °C) and put under high vacuum after the tBuOH had frozen. Supercritical-drying of the beads requires an intermediate solvent exchange into acetone (see below), after which the final exchange into $CO_2$ and subsequent supercritical-drying is performed on a supercritical-dryer (Leica EM CPD300).

The tBuOH freeze-drying and supercritical-drying ($CO_2$) require a change of solvent before the final drying process. The hydrogel beads are solvent exchanged into tBuOH or acetone in four solvent/$H_2O$ increments (25 wt-%, 50 wt-%, 75 wt-% and pure organic solvent) by placing the beads in a large excess of the most dilute solvent mixture and transferring them to the more concentrated mixture after each 24 h time increment.

## Characterization

### *Scanning Electron Microscopy (SEM) and diameter calculations*

Bead samples were placed on a carbon tape attached to aluminium SEM sample stubs, and a diamond plane was used to produce smooth beads cross-sections. Afterwards samples were then sputter coated with 5 nm of gold-platinum alloy, and subsequent SEM images were taken on a Hitachi S-

4800 Field Emission Scanning Electron Microscope (FESEM). Substructure dimensions were calculated from SEM images using ImageJ.

## *Nitrogen adsorption (BET and BJH)*

Nitrogen sorption measurements were performed on a Micromeritics TriStar II 3020 instrument at 77 K. About 40 mg of cellulose beads were placed in sample holder tubes and degassed under vacuum for 1 h. Specific surface area (SSA) was determined according to Brunauer, Emmett and Teller (BET) theory, and pore size distribution according to Barrett, Joyner and Halenda (BJH) model, applied to adsorption and desorption branches of the BET isotherm.

## *Small-angle X-ray Scattering (SAXS)*

SAXS measurements were conducted on a Double Ganesha AIR system (SAXSLAB, Denmark) operated at $\lambda = 0.154$ nm with a variable sample-to-detector distance to cover a range of scattering vectors $q = 0.002–0.5$ Å$^{-1}$. Dried samples were placed in sample holders and background scattering for empty holders was subtracted. The hydrogel SAXS profiles were measured on freshly washed samples sealed to prevent evaporation. Data reduction and azimuthal integration was performed with the instrument software. The software SasView 4.2 was used for further data analysis and Origin (2019b, OriginLab Corporation, Northampton, MA, US) for data visualisation. Porod exponents were obtained by linear fits of the log I versus log q function.

Intensity of the scattered radiation was measured as a function of magnitude of the scattering vector q to display small-angle x-ray scattering data: $q = 4\pi \sin\theta/\lambda$ typically presented in Å$^{-1}$, where $2\theta$ is the scattering angle between the incident beam and a detector, $\lambda$ is the wavelength of the x-rays. One-dimensional I(q) profiles were obtained by azimuthal averaging of 2D patterns and background subtraction. Porod exponents (PE) were determined by linear fits of log I versus log q over specified q-windows (reported below), and length scales were estimated using $d = 2\pi/q$. The relationship $I(q) \sim q^{(-PE)}$ was used to determine the Porod regime and the nature of mass and surface fractals. (Pircher et al. 2016) Thus, the value of the PE at a given range of q was used to infer whether a mass fractal dimension (PE ≈ 1-3) or a surface fractal dimension (PE ≈ 3-4) are responsible for the scattered x-ray intensity. For example, a PE value of 1 arises from rod-like 1D structures (mass fractal), 2 from 2D structures such as interlinked chains (mass fractal), value of 3 from 3D structures such as clustered networks (mass fractal) or a rough surface (surface fractal) and a value of 4 from a smooth surface (surface fractal). (Pircher et al. 2016, Plappert et al. 2018)

## *Compression testing with DMA*

The mechanical strength of the cellulose beads was recorded by uniaxial compression on a TA.XTplusC Texture Analyzer. Unconfined measurements were taken at a compression rate of 0.10 mm/s and within a conditioned environment (23 °C and 50 % of relative humidity). Measurements were taken in triplicate.

# Results and discussion

## Drying of cellulose hydrogel beads

Cellulose processing often involves steps where the polymer is soaked in a cellulose antisolvent. For example, regeneration of ionic-liquid-dissolved cellulose in water eventually results in a cellulose hydrogel. However, for many end applications and further processing steps, the presence of the antisolvent is undesirable, and a separate drying step is needed to remove it. The three common methods for drying of antisolvent-soaked regenerated cellulose are ambient drying, freeze-drying and supercritical drying. Each of the three methods relies on the removal of the antisolvent from the cellulose material, essentially only differing from each other by the nature of the phase transition the antisolvent undergoes during the process. In ambient drying the removal of antisolvent takes place via evaporation (liquid-gas phase change for antisolvent during removal) under ambient pressure and at RT or elevated temperature. In freeze-drying the removal takes place via sublimation (solid-gas phase change) under vacuum and at sub-zero temperature (depending on antisolvent, usually between -10 °C and -50 °C). While in supercritical drying the eventual removal takes place via evacuating a single supercritical phase (no phase change) under pressure and temperature required for the existence of the supercritical phase (depending on the antisolvent, e.g. >31 °C and >74 bar for the commonly used $CO_2$). Thus, the essential distinction between these drying mechanisms is in the phase boundaries, i.e. liquid-gas vs. solid-gas vs. single supercritical phase.

Cellulosic materials obtained from these three methods (supercritical-drying, freeze-drying and ambient-drying) can be broadly classified into aerogels, cryogels, and xerogels, respectively. Cellulose aerogels are characterised by a very low bulk density, high specific surface area (SSA), a high number of pores primarily in the mesoporous range (2-50 nm) as well as high pore volume. Cellulose cryogels also have a generally low bulk density, but the surface area, pore volume and the number of pores is greatly reduced due to cellulose fibre coalescence and pore collapse. The remaining porosity is primarily in the macroporous range (>50 nm) while very large macropores in the tens to hundreds of µm are often present due to ice templating (Gupta et al. 2018). In comparison to the other two, cellulose xerogels have a generally high density and because of extreme material coalescence, practically non-existent porosity and surface area. Essentially the progression from aerogel to cryogel to xerogel depicts an increase in the level of alteration and shrinkage experienced by the material during the drying process, where aerogels are closest to the morphology and nanostructure of the original hydrogel, while xerogels are the most heavily altered. However, while these broad classifications based on drying method have great utility in sorting and differentiating the various cellulose materials, the boundaries set up to segregate them are somewhat ambiguous. (Zaman et al. 2020) Consequently, the properties of two materials from adjacent classes can be more alike than those of two others within the same classification. For example, porosity-wise a cryogel freeze-dried from aq. tBuOH with a SSA of 332 $m^2 g^{-1}$ (Cai et al. 2008) is more similar to an aerogel supercritically dried from $CO_2$ with a SSA of 423 $m^2 g^{-1}$ (Beaumont et al. 2017) than it is to another cryogel freeze-dried from $H_2O$ with a SSA of 45 $m^2 g^{-1}$ (Suzuki et al. 2014).

This disparity in the preservation of the original cellulose porosity present in the hydrogel, between the SSAs of cryogels freeze-dried from neat or aq. tBuOH and those freeze-dried from $H_2O$, arises from the limited capability of the tBuOH bearing systems to grow large crystallites upon freezing. The binary mixtures of tBuOH/$H_2O$ are eutectic systems, where local minima in freezing point and also minimum in solvent crystal and tBuOH/$H_2O$ co-crystal size is reached at tBuOH concentrations of 20 % and 90 %. (Kasraian & DeLuca 1995) The forming small tBuOH crystallites are less likely to disturb or template the surrounding polymer matrix, which has straightforward benefits in preserving the pre-drying cellulose nanostructure and result in higher SSA values. For example, an increase in SSA from 94 to 220 $m^2 g^{-1}$ was observed when 10 % of tBuOH was added to the aqueous freeze-drying media, with a further increase to 319 $m^2 g^{-1}$ when the tBuOH concentration was changed to 20 %. (Nemoto et al. 2015) After this the SSA values keeps stable at ca. 300 $m^2 g^{-1}$ for compositions of 30-50 % tBuOH, but drops down to 219 $m^2 g^{-1}$ at 60 % tBuOH. In contrast, in a purely aqueous medium the formation of large $H_2O$ crystallites is much more intrusive on the hydrogel cellulose matrix, which results in high levels of cellulose coalescence during the drying process. One may expect that SSA and mesopore volume decrease in the order of aerogels > tBuOH-cryogels > $H_2O$-cryogels >> xerogels. This may be confirmed by means of X-ray scattering: e.g. Porod exponents and characteristic q-shifts reflect increasing consolidation (shift to lower q

indicates growth of characteristic features). On the other hand, electron and optical microscopy should visualize pore wall substructures decrease in definition from aerogel to $H_2O$-cryogel to xerogel as fibrils coalesce and pore walls thicken.

Therefore, in this study four separate methods have been used in drying hydrogel beads prepared from aqueous regeneration of [DBNH][OAc]/DMSO dope: supercritical drying from $CO_2$, freeze-drying from tBuOH, freeze-drying from $H_2O$, and ambient drying from $H_2O$. As a consequence of the different drying processes, significant changes are observed in the physical properties and appearance of the resulting dry materials. The aero- and cryogel beads retain their hydrogel dimensions and acquire a white opaque colour, while during the ambient-drying process leading ultimately to xerogel beads, the hydrogel beads will change appearance from whitish opaque to transparent and shrink to roughly one-third of their original diameter. The intermediate stages of shrinkage are also intermediate in their change of appearance, turning more and more towards transparent the smaller the bead gets (Figure 1).

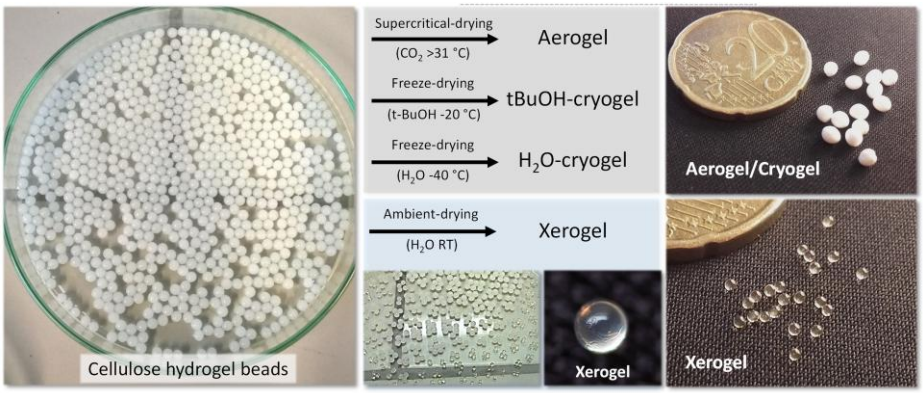



**Fig. 1** A scheme illustrating changes taking place in the general appearance of the cellulose hydrogel beads during the different drying methods resulting in aerogel, cryogel and xerogel beads. The transformation of the large whitish opaque hydrogel beads into the smaller transparent xerogel beads is a gradual process and the changing appearance of the drying beads is indicative of the decreasing water content. This change in appearance and water content from hydrogel to xerogel correlates with an increase in density.

## SEM

Low magnification Scanning Electron Microscope (SEM) images of cross-sections of the aerogel, cryogel and xerogel beads are shown in Figure 2. The internal cellulose matrix of the aerogel and tBuOH-cryogel beads was more delicate than that of the $H_2O$-cryogel and xerogel beads and less resistant to the shear induced by the cutting blade of the diamond plane, and hence a more ragged cross-section was obtained after dissection. As can be observed from the mechanical compression data later in this article, the hydrogel and cryogel beads are weak, while the xerogel beads are significantly stronger and tough.

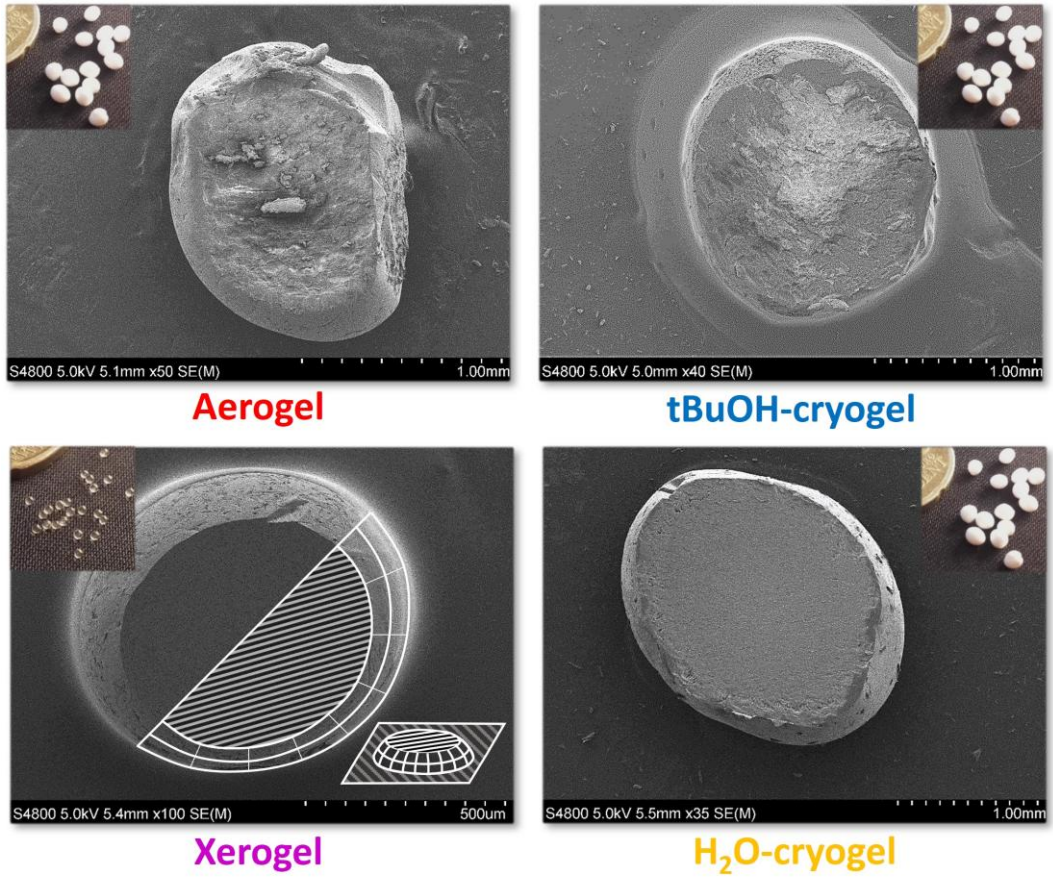



**Fig. 2** SEM micrographs of the cross-sections of the four different types of dried beads. The internal structure of the aerogel and tBuOH-cryogel beads was more delicate than that of the $H_2O$-cryogel and xerogel beads and hence a more ragged cross-section was obtained after bisection. Note the different scale on the xerogel bead (scalebar 500 µm vs 1.00 mm for the others).

Under high magnification (Figure 3), the three porous bead types (aerogel and the two cryogels) all display internal morphology typical of a dried regenerated cellulose matrix, with the solid cellulose matrix of the pore walls surrounding roughly spherical pores of various sizes (meso- to macropores). A marked difference can be observed in the internal structure of the xerogel beads in comparison, the matrix is considerably more compacted and of significantly lower porosity than the other bead types, albeit a contributing factor to the observed smoothness of the surface is a certain level of polishing induced by the cutting action of the plane blade during sample preparation. The $H_2O$-cryogel also has distinctly larger pores, thicker pore walls and in general more coarse structure in comparison to aerogel and tBuOH-cryogel, which are more delicate and in the case of the aerogel, even fibrous. This is a clear indication of the large differences in the degree of cellulose coalescence taking place during the different processes used in drying the hydrogel, the degree increasing in the order aerogel → tBuOH-cryogel → $H_2O$-cryogel → xerogel.

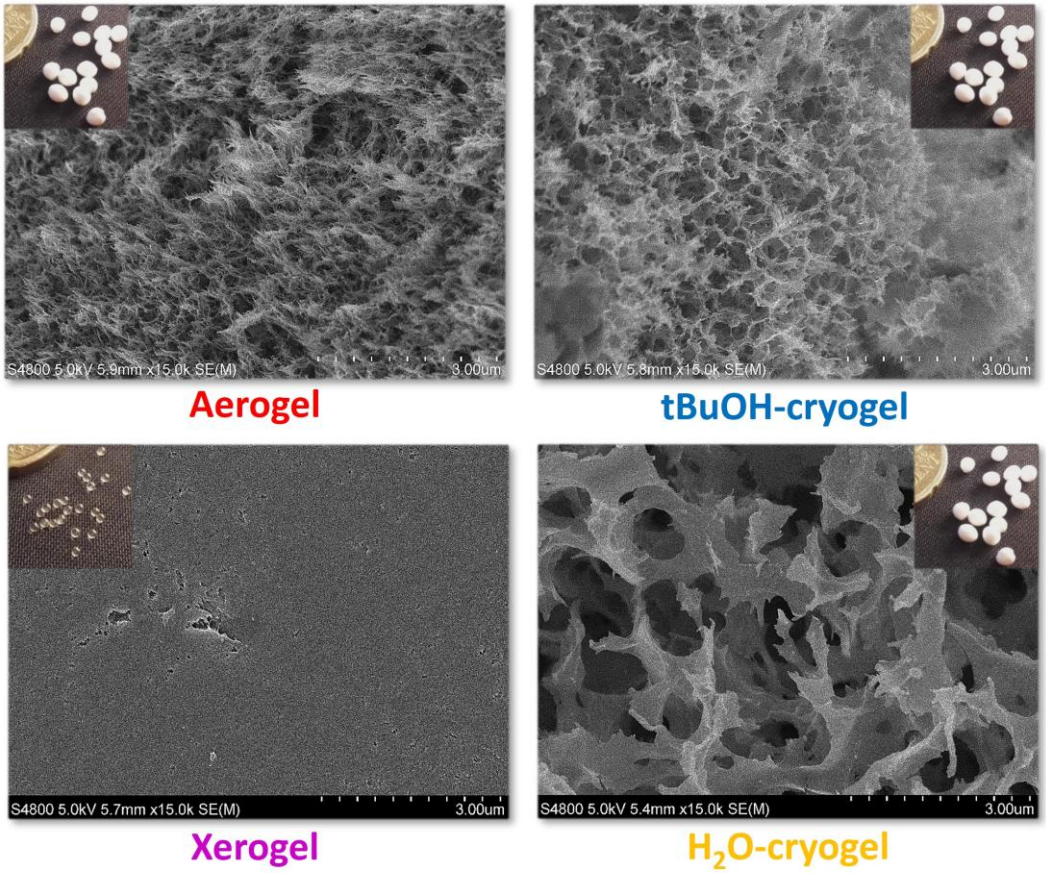



**Fig. 3** High magnification SEM micrographs of the cross-sections of the four types of beads. The xerogel beads exhibit significantly more compacted and less porous internal structure compared to the other bead types.

## Analysis of porosity and pore size distribution

Determination of the specific surface area (SSA) with the BET (Brunauer-Emmett-Teller) gas adsorption method and the pore size distribution and pore volume via the BJH (Barrett-Joyner-Halenda) method are often utilized in characterizing porous cellulose materials. In comparative terms the values can be also used to assess the impact of the regeneration and drying methods, as well as the effect of possible pre- and post-treatments. A series of solvent, regeneration and drying method, SSA, average pore size, and bulk density values for various cellulosic materials reported in the scientific literature is collected in Table 1.

**Table 1.** Reported values for specific surface area (SSA with BET), average pore size (with BJH) and bulk density for cellulose materials regenerated from a wide range of solvent systems and using various regeneration and drying methods.

| Cellulose material | Solvent system | Processing /regene-ration method | Drying method | SSA, $m^2/g$, BET | Average pore size, nm, BJH | Bulk density, $mg/cm^3$ | Ref. |
|---|---|---|---|---|---|---|---|

| | | | | | | | |
|---|---|---|---|---|---|---|---|
| Aerogel | [TMGH][OAc] | Antisolvent regeneration (EtOH) | Supercritical -drying ($CO_2$) | 396 - 633 | - | 15 - 80 | Plappert 2018 |
| Aerogel | - | TEMPO-oxidation | Supercritical -drying ($CO_2$) | 500 - 600 | - | - | Kobayashi 2014 |
| Aerogel | [bmim]Cl | Antisolvent regeneration (aq. EtOH, 90 %) | Supercritical -drying ($CO_2$) | 539 | - | - | Aaltonen & Jauhiainen 2009 |
| Aerogel | aq. NaOH/urea & aq. LiOH/urea | Antisolvent regeneration (EtOH) | Supercritical -drying ($CO_2$) | 260 - 485 | 8 - 39 | - | Cai 2008 |
| Aerogel | aq. NaOH/urea | Antisolvent regeneration (aq. $HNO_3$ or aq. NaCl) | Supercritical -drying ($CO_2$) | 340 - 470 | - | - | Trygg 2013 |
| Aerogel | - | Mechanical refining (230-34 000 kWh $ton^{-1}$) | Supercritical -drying (EtOH) | 199 - 430 | - | - | Moser 2016 |
| Aerogel | [bmim]Cl | Thermal gelling + EtOH washes | Supercritical -drying ($CO_2$) | 336 - 426 | 13 - 28 | 16 - 55 | Lin & Jana 2021 |
| Aerogel | NMMO·$H_2O$ | Workup (aq.) + high-pressure homogenization | Supercritical -drying ($CO_2$) | 423 | 35 | - | Beaumont 2017 |
| Aerogel | [bmim]Cl | Antisolvent regeneration ($H_2O$) | Supercritical -drying ($CO_2$) | 382 | 34 | - | Zeng 2020 |
| Aerogel | [bmim][OAc] | Antisolvent regeneration (EtOH) | Supercritical -drying ($CO_2$) | 348 | 34 | - | Zeng 2020 |
| Aerogel | TBAF/DMSO 17:83 | Antisolvent regeneration (EtOH) | Supercritical -drying ($CO_2$) | 328 | - | 70 | Pircher 2016 |
| Aerogel | [bmim][OAc] | Antisolvent regeneration ($H_2O$) | Supercritical -drying ($CO_2$) | 306 | 14 | - | Zeng 2020 |
| Aerogel | $Ca(SCN)_2·4H_2O$ | Antisolvent regeneration (EtOH or iPrOH) | Supercritical -drying ($CO_2$) | 287 - 303 | - | - | Ganesan 2016 |
| Aerogel | [DBNH][$CO_2$Et] | Antisolvent regeneration ($H_2O$, EtOH or iPrOH) | Supercritical -drying ($CO_2$) | 238 - 302 | - | - | Druel 2018 |
| Aerogel | aq. NaOH | Thermal gelling + aq. washes | Supercritical -drying ($CO_2$) | 200 - 300 | - | 60 - 300 | Gavillon & Budtova 2008 |
| Aerogel | NMMO·$H_2O$ | Antisolvent regeneration ($H_2O$ or EtOH) | Supercritical -drying ($CO_2$) | 172 - 284 | 11 - 13 | 50 - 260 | Liebner 2008 |

| | | | | | | | |
|---|---|---|---|---|---|---|---|
| Aerogel | $NMMO{\cdot}H_2O$ | Antisolvent regeneration (EtOH) | Supercritical-drying ($CO_2$) | 250 | - | 60 | Pircher 2016 |
| Aerogel | [emim][OAc]: DMSO 30:70 | Antisolvent regeneration (EtOH) | Supercritical-drying ($CO_2$) | 246 | - | 40 - 60 | Pircher 2016 |
| Aerogel | [amim]Cl | Antisolvent regeneration (aq. [amim]Cl) | Supercritical-drying ($CO_2$) | 176 - 244 | 23 - 26 | 24 - 30 | Mi 2016 |
| Aerogel | [emim][OAc] | Antisolvent regeneration ($H_2O$) | Supercritical-drying ($CO_2$) | 130 - 230 | 10 - 15 | - | Sescousse 2011 |
| Aerogel | $Ca(SCN)_2{\cdot}8H_2O$/ LiCl | Antisolvent regeneration (EtOH) | Supercritical-drying ($CO_2$) | 190 | - | 30 - 50 | Pircher 2016 |
| Cryogel | aq. LiBr | Thermal gelling + aq. washes | Freeze-drying (tBuOH) | 221 - 400 | 7 - 8 | 5 - 120 | Liao 2019 |
| Cryogel | - | Mechanical refining + aq. HCl gelling | Freeze-drying (tBuOH) | 338 - 349 | - | 5 | Saito 2011 |
| Cryogel | aq. LiOH/urea | Antisolvent regeneration (EtOH) | Freeze-drying ($H_2O$/tBuOH mixture)* | 332 | - | - | Cai 2008 |
| Cryogel | - | Mechanical refining + TEMPO-oxidation | Freeze-drying ($H_2O$/tBuOH mixture)* | 219 - 319 | - | - | Nemoto 2015 |
| Cryogel | $NMMO{\cdot}H_2O$ | Workup (aq.) + high-pressure homogenization | Freeze-drying (tBuOH) | 298 | - | - | Beaumont 2016 |
| Cryogel | - | TEMPO-oxidation and/or mechanical refining | Freeze-drying ($H_2O$/tBuOH mixture)* | 153 - 284 | 11 - 16 | - | Sehaqui 2011 |
| Cryogel | $Ca(SCN)_2{\cdot}4H_2O$ | Antisolvent regeneration (MeOH) | Freeze-drying (tBuOH) | 160 - 190 | - | - | Jin 2004 |
| Cryogel | [bmim]Cl | Antisolvent regeneration ($H_2O$) | Freeze-drying (tBuOH) | 181 | - | - | Deng 2009 |
| Cryogel | aq. LiOH/urea | Antisolvent regeneration (EtOH) | Freeze-drying ($H_2O$) | 142 | - | - | Cai 2008 |
| Cryogel | aq. NaOH/urea | Antisolvent regeneration (aq. HCl + $CaCl_2$) + TEMPO | Freeze-drying ($H_2O$) | 59 - 132 | - | - | Lin 2017 |
| Cryogel | - | NaOH & $NaClO_2$ washes | Freeze-drying (tBuOH) | 130 | - | - | Ishida 2004 |

| | | | | | | | |
|---|---|---|---|---|---|---|---|
| Cryogel | $Ca(SCN)2{\cdot}4H_2O$ | Antisolvent regeneration (MeOH) | Freeze-drying ($H_2O$) | 70 - 120 | - | - | Jin 2004 |
| Cryogel | - | TEMPO-oxidation | Freeze-drying ($H_2O$) | 94 | - | - | Nemoto 2015 |
| Cryogel | [bmim]Cl/DMF | Emulsification (hexane/ surfactant) + washes | Freeze-drying ($H_2O$) | 45 | - | - | Suzuki 2014 |
| Cryogel | - | NaOH & $NaClO_2$ washes | Freeze-drying ($H_2O$) | 25 | - | - | Ishida 2004 |
| Cryogel | [emim][OAc]: DMSO 30:70 | Antisolvent regeneration (MeOH or $H_2O$) | Freeze-drying ($H_2O$) | - | - | 17 - 22 | Johns 2017 |
| Xerogel | [bmim]Cl/DMF | Emulsification (hexane/ surfactant) + washes | Ambient-drying ($H_2O$) | 0.4 | - | | Suzuki 2014 |
| Xerogel | LiCl/DMAc | Antisolvent regeneration (EtOH) | Ambient-drying ($H_2O$) | - | - | 1400 | Li 2020 |

* In some reports, eutectic $H_2O$/tBuOH mixtures were used in freeze-drying. Authors propose that, e.g., 10/90 composition is optimal mixture for freeze-drying and produces the smallest crystal size upon freezing. (Kasraian & DeLuca 1995)

As can be clearly observed in Table 1, the three different drying methods and their corresponding end materials can be distinguished from each other based on their BET SSA values. Supercritically dried aerogels occupy a range of high SSA values between 630 and 130 $m^2\ g^{-1}$ based on experimental and treatment history, with common values between 450 and 250 $m^2\ g^{-1}$. On the other hand, cryogels occupy a lower range of values between 400 and 25 $m^2\ g^{-1}$, where cryogels freeze-dried from neat or aq. tBuOH reside in the higher end 400 to 150 $m^2\ g^{-1}$, while those freeze-dried from $H_2O$ reside in the lower end 142 to 25 $m^2\ g^{-1}$. When both tBuOH-cryogels and $H_2O$-cryogels were analysed within the same study, the SSA of the $H_2O$-cryogels were found to be between 19 % and 55 % of the corresponding tBuOH-cryogel: 25 $m^2\ g^{-1}$ vs 130 $m^2\ g^{-1}$ (Ishida et al. 2004), 70-120 $m^2\ g^{-1}$ to 160-190 $m^2\ g^{-1}$ (Jin et al. 2004) and 142 $m^2\ g^{-1}$ to 332 $m^2\ g^{-1}$ (Cai et al. 2008). Clearly separate from the other two types of dried materials, xerogels exhibit a distinctly low SSA value characteristic of their practically non-porous nature, the singular example listed here having a meagre surface area of 0.4 $m^2\ g^{-1}$. These various types of dry materials mostly occupy discrete SSA value ranges, with the most significant overlap being present at the lower range of aerogels and the higher range of the tBuOH cryogels. This broad spread of values clearly demonstrates that the SSA of a dry cellulose material is exceedingly determined by the treatment history of the sample rather than by possible differences in the chemical substitution or degree of polymerization of the polymer itself. Analysis of this data allows one to summarize SSA value ranges for aerogels as 130-630 $m^2\ g^{-1}$, for tBuOH-cryogels as 150-400 $m^2\ g^{-1}$, for $H_2O$-cryogels as 25-142 $m^2\ g^{-1}$, and for xerogels as ~0-1 $m^2\ g^{-1}$. Our data are consistant with Table 1 values.

Besides the distinctly different drying methods and choice of drying solvent, other physical factors and process parameters can also have an effect on the SSA value of a dry cellulose material. One very apparent yet particularly influential factor is the number of cellulose molecules present at a given unit volume of dry material, which in the case of regeneration by addition of antisolvent is usually directly correlated with cellulose concentration in the dope. Higher dope concentration leads to higher number of molecules in any given volume, and inversely as lesser number of non-cellulose molecules (eventually pores). Additionally, a higher volume concentration of cellulose during the drying process leads to more pronounced fibre coalescence, further limiting SSA. A 37 % drop in SSA from 633 to 396 $m^2\ g^{-1}$ was observed when cellulose concentration in [TMGH][OAc] was increased from 1 to 3 wt-%, (Plappert et al. 2018) while a 43 % drop from 230 to 130 $m^2\ g^{-1}$ was

observed when cellulose concentration in [emim][OAc] was increased from 3 to 15 wt-%. (Sescousse et al. 2011) Similarly, the average BJH mesopore size decreased from 15 to 10 nm when the cellulose concentration increased from 5 to 10 wt-%. (Sescousse et al. 2011) When a drying method requiring a solvent exchange step is employed, the number of solvent exchange steps can have a marked effect on the resulting SSA. This was observed when the number of steps in the $H_2O$ to tBuOH solvent exchange was increased from 1 to 6, resulting in a 12 % increase in SSA for TEMPO-oxidized cellulose (254 to 284 $m^2$ $g^{-1}$) and a significant 63 % increase for unmodified cellulose (153 to 249 $m^2$ $g^{-1}$). (Sehaqui et al. 2011)

A common strategy, for avoiding the strong capillary forces water applies on a cellulose structure during evaporation, has been to use solvent exchange before drying. Drastic pore closure during evaporative drying of both wood and paper fibres from water leads to very low porosities (<0.002 $cm^3$ $g^{-1}$) and surface areas (1 $m^2$ $g^{-1}$), but when water is exchanged to pentane via methanol and the fibres were dried evaporatively, the values of two different fibres, wood and paper, differed to a very large degree as a result: the porosity and surface area of the paper fibres (0.4 $cm^3$ $g^{-1}$, 230 $m^2$ $g^{-1}$) were 50 to 70 times higher than those of the wood fibres (0.006 $cm^3$ $g^{-1}$, 5 $m^2$ $g^{-1}$). (Stone & Scallan 1965) These disparate values highlight the dramatic impact the high surface tension of water as a drying solvent has on cellulose pore collapse during drying, and evidence the space filling effect the non-cellulose components in wood have on the overall structure and porosity. These differences in surface area and mesoporosity suggest distinct nanoscale organizations, which we probed by SAXS.

## BET and BJH

The specific surface area (SSA), pore size distribution and pore volume of the cellulose beads prepared in this study were determined by nitrogen adsorption-desorption analysis via the BET (Brunauer-Emmett-Teller) and BJH (Barrett-Joyner-Halenda) methods. The adsorption and desorption isotherms and the pore volume analysis of the aerogel and cryogel beads are shown in Figure 4. The isotherm data for the practically non-porous xerogel beads is not shown due to extremely low SSA value (0.036 $m^2$ $g^{-1}$), while all of the other three types of beads exhibit type II adsorption-desorption isotherms with type H3 hysteresis loops according to IUPAC classifications (Thommes et al. 2015), characteristic of an adsorbent comprised of both meso- and macropores. The isotherm type for the $H_2O$-cryogel beads is difficult to discern from the graph due to very low adsorption quantity. However, when viewn separately, the isotherm shape is similar to the other two shown (type II). A gently curving inflection point B is visible in the isotherm of the aerogel beads (red isotherm) at a value of 0.02-0.03 p/p°, corresponding to a significant overlap in monolayer completion and onset of multilayer adsorption.

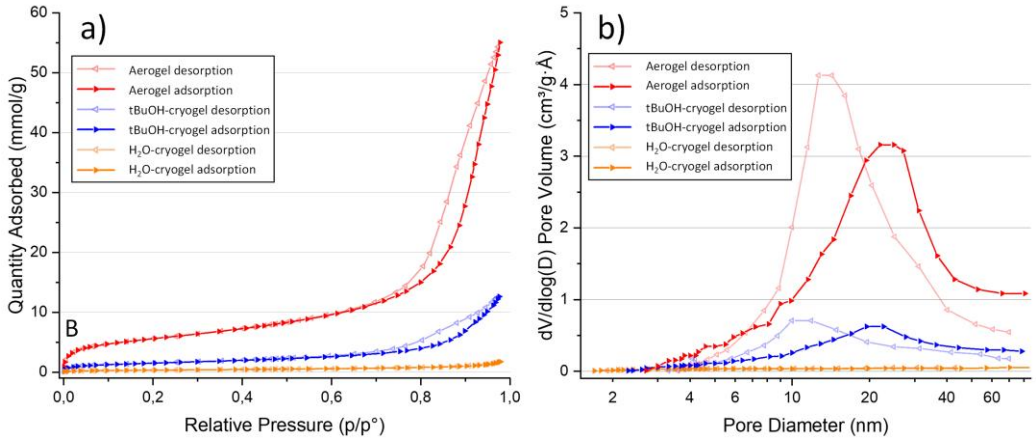



**Fig. 4 a)** BET adsorption (solid right facing arrow heads) and desorption isotherm data (open left facing arrow heads) for the aerogel and cryogel beads. Xerogel beads (not pictures) were shown to be practically non-porous. Aerogel and cryogels exhibit type II isotherms with H3 hysteresis loops.

(Thommes et al. 2015) **b)** BJH pore volume analysis of the adsorption and desorption isotherm of aerogel and cryogel beads. An adsorption average mean mesopore diameter of 17.5 nm for the aerogel and 15.2 nm for the tBuOH-cryogel is calculated from the isotherm data. The pore diameter with the largest contribution to the total mesopore volume is indicated by the peak maximum and is found at ca. 21 nm for both aerogel and tBuOH-cryogel. $H_2O$-cryogel has an adsorption average mesopore diameter of 9.1 nm but does not exhibit a clear peak maximum.

Values of specific surface area (SSA), mesopore volume and average mesopore diameter measured from the adsorption branch of the nitrogen isotherm data of the various cellulose beads are shown in Table 2. The disparity in surface area between the different cellulose beads is very pronounced: the aerogel beads with a SSA of 450 $m^2 g^{-1}$ having roughly four times the surface area of the tBuOH-cryogel beads (123 $m^2 g^{-1}$) and 16 times that of the $H_2O$-cryogels beads (29 $m^2 g^{-1}$). The SSA of the xerogel beads at a value of 0.04 $m^2 g^{-1}$ is more than 700 times smaller than even the $H_2O$-cryogels beads, which makes the xerogel beads essentially non-porous in this context. Comparison of typical SSA ranges for regenerated cellulose after different drying routes (Table 1, literature ranges) and values for this work demonstrates: i) aerogels (supercritical $CO_2$): 130-630 $m^2 g^{-1}$ (typical 250-450), this work: 450 $m^2 g^{-1}$; ii) cryogels (tBuOH freeze-drying): 150-400 $m^2 g^{-1}$, this work: 123 $m^2 g^{-1}$; iii) cryogels ($H_2O$ freeze-drying): 25-142 $m^2 g^{-1}$, this work: 29 $m^2 g^{-1}$; 4) xerogels (ambient evaporation): ~0-1 $m^2 g^{-1}$, this work: 0.04 $m^2 g^{-1}$. In comparison to materials prepared in other studies, the SSA of the aerogel beads represent a high-average value for supercritically dried cellulose, while the SSA of the tBuOH-cryogel beads represents a low-average value for tBuOH-freeze-dried materials. One must note that SSA depends strongly on polymer concentration in the dope, regeneration and solvent exchange protocols, and drying history. For further comparison, the SSA of a MD simulated 24-chain cellulose microfibril is 870 $m^2 g^{-1}$, while that of a bundle composed of four microfibrils is somewhat lower at 520-630 $m^2 g^{-1}$ (dynamic).(Paajanen et al. 2019)

Similarly to the surface area, the pore volume data highligths the relative difference in the surface texture of the different dry beads. While the total mesopore volume of the aerogel (1.98 $cm^3 g^{-1}$) is much larger than the cryogels (0.45 $cm^3 g^{-1}$ for tBuOH-cryogel and 0.06 $cm^3 g^{-1}$ for $H_2O$-cryogel), both the aerogel and tBuOH-cryogel have a broad distribution of mesopores between 4 and 50 nm, with an adsorption average mesopore diameter at 17.5 nm and 15.2 nm respectively. Also, the pore diameter with the largest contribution to total mesopore volume is indicated by the peak maximum, which is ca. 21 nm for both aerogel and tBuOH-cryogel. While the adsorption isotherm of the $H_2O$-cryogel gives an adsorption average mesopore diameter of 9.1 nm, the distribution of the mesopores does not indicate a single peak maximum. However, it should be noted that the BJH method is only capable of effectively determining the nano- and mesoporosity of a sample matrix (<200 nm pore size, here shown between 2 and 80 nm), which leaves a major and often the largest contributor to cellulose aerogel porosity and pore volume, the macropores, outside of many considerations. (Robitzer et al. 2011)

**Table 2.** BET specific surface area (SSA) and BJH mesopore volume (MV) for the various types of cellulose beads. Peak mesopore diameter (PMD) refers to BJH adsorption branch.

| **Sample** | **SSA**, $m^2/g$ | **MV**, $cm^3/g$ | **PMD**, nm |
|---|---|---|---|
| Aerogel | 450 | 1.98 | 21 |
| tBuOH-Cryogel | 123 | 0.45 | 21 |
| $H_2O$-Cryogel | 29 | 0.06 | - |
| Xerogel | 0.036 | - | - |

## Effect of drying on cellulose pore morphology, regeneration-derived spherical substructures

To better understand how the hydrogel's demixing-derived mesostructure survives drying, we examined regeneration-derived spherical substructures across beads and linked them to SAXS features. Even though nucleation-based phase separation mechanisms should generally become dominant only in very polymer-rich or polymer-poor systems undergoing slow compositional changes, in some instances cellulose regenerating via presumably fast spinodal decomposition assembles itself in the shape of roughly spherical substructures, such as was the case with antisolvent induced regeneration from molten NMMO·$H_2O$, (Gavillon & Budtova 2008) [emim][OAc], (Sescousse et al. 2011) or [emim][OAc]/DMSO (Pircher et al. 2016). While these substructures have been previously attributed to spinodal decomposition, (Gavillon & Budtova 2008) similar structures were formed from the same [emim][OAc]/DMSO system also upon cooling, solidifying or just standing, which would imply either an inherently unstable system, significantly reduced demixing rate or a phase separation mechanism based on a slower nucleation derived process.

At certain places within the dry beads prepared in this study, spherical cellulose morphology can be observed (Figure 5). This morphology is most apparent in the aerogel, but similar structures are also observed in the tBuOH-cryogel and xerogel materials, while they seem to be absent in the $H_2O$-cryogel. Found in groups, in the aerogel these 500-700 nm structures (average diameter 570 nm) resemble a jumble of stacked spheres and their surface appears pilose. In comparison, in the tBuOH-cryogel the analogue structures, slightly smaller at 400-600 nm (average diameter 530 nm), resemble a more node-like assemblage of spheres connected by struts and their surface appears distinctly more prickly, i.e. roughened fibrillar protrusions of ~35-60 nm. Even though the corresponding spherical structures are not easily observed on the xerogel cross-section due to surface polishing taking place during dissection, groups of smooth 20-30 nm diameter (average 27 nm) spheres can be found on the inside walls of some of the very few larger porous defects present in the otherwise dense and non-porous matrix. In other words, we interpret the ~0.5-0.7 µm clustered spherical domains in aerogels as preserved blobs arising during liquid-liquid demixing (spinodal-like) during antisolvent ingress in [DBNH][OAc]/DMSO systems, consistent with [Sescousse et al. 2011; Gavillon & Budtova 2008; Pircher et al. 2016]. While our data does not support the slower nucleation-and-growth -derived mechanism in SBIL/OES systems, we propose it may contribute depending on local composition, kinetics, and type of regeneration (antisolvent vs thermal).

During drying, the relatively unfused cellulose structures (such as fibril ends) found in the hydrogel are forced together into larger bundles and a more condensed form by a range of processes such as capillary forces and formation of solvent crystals. The SEM micrographs succeed in illustrating the varying degree of such structural alteration imparted on the cellulose framework depending on the drying method. The degree can be observed to increase in the order aerogel → tBuOH-cryogel → $H_2O$-cryogel → xerogel. In particular, the transformation of the pilose spherical substructures found in aerogel, first into the prickly nodes in tBuOH-cryogel and finally into tightly fused flat pore walls in $H_2O$-cryogel, clearly demonstrates the increasing degree of consolidation taking place during the freeze-drying methods. For example, the fibril ends making up the pilose rough surface of the aerogel substructures are on average 35 nm in diameter, whereas the analogue fibrils in the tBuOH-cryogel are already 60 nm in diameter and no comparative structures can be found in the $H_2O$-cryogel. This trend of increasing consolidation is taken to its natural extreme by the xerogel material, being composed solely of a dense, non-porous mass of cellulose with no apparent signs of the formerly porous matrix.

For comparison, the calculated cross-sectional area of a single cellulose chain is 0.32 $nm^2$ (Zhao et al. 2013) and the measured average diameter of the chain is 0.6 nm (0.4×0.83 nm) (Song et al. 2020). The diameter of larger cellulose structures such as a cellulose I microfibril in higher plants is in the order of 3-4 nm, depending somewhat on the biological source and function. The exact number of cellulose chains in the microfibril is not exactly known, but a model containing either 18 or 24 cellulose chains per fibril seems to best fit available data.(Fernandes et al. 2011, Paajanen et al. 2019, Allen et al. 2021) However, these microfibrils often aggregate together into larger bundles sometimes up to 50 nm wide,(Song et al. 2020) whereas very narrow microfibrils down to 1 nm can also be found, when the biological function of the fibril is not to provide strength and rigidity, such as in fruit tissue.(Niimura et al. 2010) Therefore, a common range of diameter of 3-4 nm for individual fibrils to few tens of nm for fibril bundles can be expected for cellulose I sourced from

higher plants. In general, lower plants, bacteria, and tunicates biosynthesize considerably thicker microfibrils in the range of 10-50 nm.(Niimura et al. 2010)

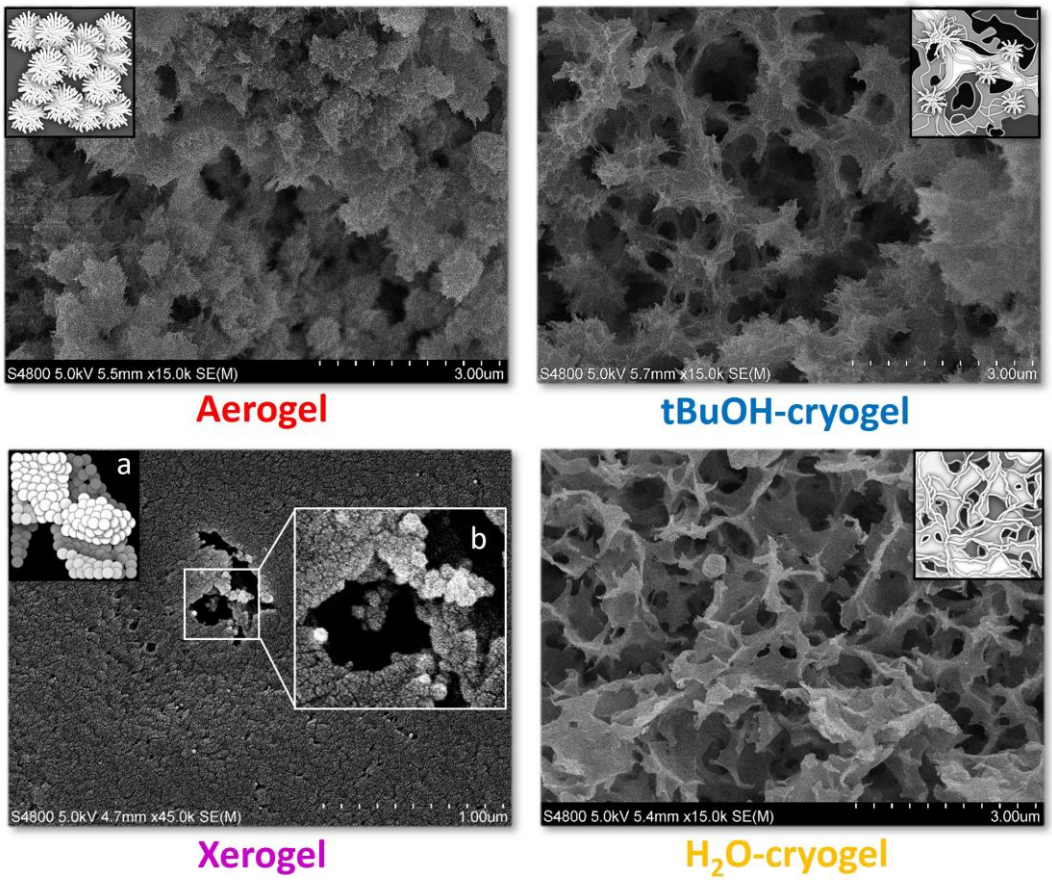



**Fig. 5** SEM micrographs of the cross sections of the four types of beads. Inset in the top corner of each micrograph depicts the prevailing shape of the cellulose matrix observed (in case of xerogel inset a). Roughly spherical substructures can be found in the aerogel, tBuOH-cryogel and xerogel, while no clear indication of such structures can be found in $H_2O$-cryogel. Xerogel inset b depicts a zoomed-in portion of the micrograph, with visible microstructure inside the porous defect in the otherwise non-porous matrix. Note the different scale in xerogel.

The formation of the spherical cellulose substructures within regenerating solutions seems to require a certain level of cellulose mobility, as none have been observed to form in already solidified (NMMO·$H_2O$) or gelled (NaOH) mixtures. In the case of these solidified and gelled mixtures, cellulose movement has been restricted by either a partial (NMMO·$H_2O$) (Gavillon & Budtova 2008) or full phase separation (NaOH) (Demilecamps et al. 2014). This confinement into a separate and much less voluminous phase necessitates that the cellulose chains adopt a much more spatially compact packing, which results in a partly pre-determined matrix structure for cellulose even before the terminal regeneration by antisolvent. However, when a single-step phase separation occurs in a true cellulose solution, the spatially even but random distribution of cellulose chains enables the formation of "random" low-density spheres. However, mobility is not the only factor controlling the formation of these spheres, as most alkali hydroxide solutions of cellulose do not form them even when the mixture is not allowed to gel before regeneration (Budtova 2019).

## Small-angle X-ray scattering, SAXS

Small Angle X-ray Scattering (SAXS) was used to study the nanoscale organization and interfacial morphology of crystalline and amorphous cellulose in the beads after different drying routes.

A study on cellulose regeneration (Nishiyama et al. 2019) from both [DBNH][OAc] and NMMO·$H_2O$ dopes by in situ monitoring via simultaneous scanning SAXS-WAXS instrument provides a glimpse on how the different characteristics of these two solvents (outlined in section Regeneration of cellulose) manifest as distinct nano-scale structures during regeneration in bulk objects. Before any antisolvent ($H_2O$) has been added, NMMO·$H_2O$/cellulose dope scattering intensity in SAXS follows a power law exponent -3 at $q \leq 0.008$ Å$^{-1}$, which implies that a certain level of inhomogeneity already existed in the dope even before regeneration. This inhomogeneity could arise from possible presence of microcavities in the dope or from crystalline domains observed in the WAXS range. During regeneration these crystalline domains recede at roughly 5 % $H_2O$ while diffraction peaks (d-spacings 4.5 Å and 4.2 Å) resembling cellulose II (110 = 4.4 Å and 020 = 4.0 Å) emerge starting at 10-15 % $H_2O$. This is later followed by the emergence of diffraction peak at 1.4 Å$^{-1}$ alongside SAXS characteristic of cellulose nanofibrils clearly separate from the solvent (power law for scattering between q = 0.1-0.2 Å$^{-1}$ is almost -4). In a range q = 0.01 - 0.06 Å$^{-1}$, the scattering follows a -2 power law, which together with high directionality of the crystallization indicated the presence of flat structures. A simulated scattering of a ribbon with dimensions of 200 × 40 × 2 nm resembled the scattering profile of the experimental sample to a very high degree, especially at $q \leq 0.07$ Å$^{-1}$.(Nishiyama et al. 2019)

On the other hand, unregenerated [DBNH][OAc] dope did not exhibit the same structural inhomogeneity as the NMMO·$H_2O$ and the scattering intensity below q = 0.04 Å$^{-1}$ followed a power law exponent of -1. Also differing from NMMO·$H_2O$, regeneration from [DBNH][OAc] resulted in significant intensity increase below q = 0.1 Å$^{-1}$, the process beginning with the appearance of a feature around 0.015 Å$^{-1}$ (density fluctuation with a ca. 40 nm periodicity) at 5 % $H_2O$. The process appeared to have finishing at 15 % $H_2O$, as no increase in small angle scattering intensity was observed after that. It was suggested that these density fluctuations were most likely arising from phase separation of the system via spinodal decomposition. Also noteworthy was that no noticeable crystalline peaks appeared in the WAXS range during the whole process, which is in contrast with previous results of fibre spinning from [DBNH][OAc] dopes, where a crystallinity of between 28-36 % was obtained depending on the draw ratio. (Sixta et al. 2015, Hauru et al. 2016) This implies that the cellulose crystallinity observed in fibres spun from [DBNH][OAc] can be mostly attributed to the draw-induced shear in the air gap, instead of it being an inherent outcome of regeneration. Additionally, some crystallinity of the end product likely arises from cellulose reorganisation during the washing and possible drying processes, which were not observable in the Nishiyama et al. study as the sample was not washed or dried during the measurement.(Nishiyama et al. 2019)

Plappert et al. (Plappert et al. 2018) prepared large scale cellulose objects by placing hot cellulose/[TMGH][OAc] dope inside EtOH-soaked cylindrical moulds and regenerating the contents in place via further addition of EtOH. The resulting material was studied using SAXS and it was found that the nanofibrous cellulose matrix had a cross-sectional Guinier radius ($R_g$) of 2.5 nm in the interior of the object, while a slightly larger 3.0 nm was observed in the 1 mm outer skin (cylinder radius 22 mm). This larger value in the skin was attributed to rapid initial cellulose coagulation around the mould edges during immersion.

During drying, SAXS analysis revealed markedly different structural evolution pathways for cellulose hydrogels and alcogels. Hydrogel beads underwent a three-stage evolution, whereas alcogel beads exhibited only gradual changes between the initial and final states. Guinier–Porod analysis identified two characteristic scattering features ($R_{g1} \approx 0.5–1.2$ nm and $R_{g2} \approx 2.2–14.5$ nm), corresponding approximately to cellulose monomers and their elongated aggregates. The initial nanostructure of both materials consisted of a lamellar-like network of cellulose chains containing these aggregates. During hydrogel drying, this network underwent slight initial consolidation, rapid transformation into spherical aggregates, and subsequent formation of rod-like structures within larger aggregates, whereas the size and morphology of the scattering features remained largely unchanged in alcogels. These results demonstrate that drying induced consolidation is accompanied by extensive nanostructural reorganization in hydrogels but only minor structural changes in alcogels (Li et al. 2020).

Our results do not contradict to the previously published observations and correspond to the fully dried cellulose particles. All dried samples showed power-law regimes in the SAXS profiles, with Porod exponents reflecting interfacial roughness and consolidation, see Figure 6. Aerogels exhibited PE ≈ 3.5-3.8 in the range $0.01 < q/Å^{-1} < 0.2$, indicative of relatively rough interfaces consistent with an open, fibrillar mesoporous network. The tBuOH cryogels showed intermediate behavior (PE ≈ 3.7-3.9 over similar q), while $H_2O$ cryogels approached a near-Porod regime (PE ≈ 3.9-4.0), consistent with smoother, more coalesced interfaces and thicker pore walls. Xerogels displayed a diminished small-angle intensity and an extended $q^{-4}$ regime (PE ≈ 3.9-4.0), in agreement with their dense, essentially non-porous character from gas sorption.

Subtle slope changes were detected near $q \approx 0.021$ $Å^{-1}$ and $q \approx 0.010$ $Å^{-1}$, corresponding to real-space length scales $d \approx 2\pi/q \approx 30$ nm and ≈ 63 nm, respectively, see Figure 6. Features at ~30 nm were evident in aerogels and tBuOH cryogels and persisted, albeit modified, in xerogels. A roughly similar sized feature is possibly also present in the never-dried and freeze-dried tBuOH-cryogel beads. However, whether this feature is of same origin in the three bead types is questionable, as the air-dried beads have undergone severe dimensional shrinkage and reordering of cellulose chains in comparison to the never-dried and freeze-dried tBuOH beads. In contrast, the $H_2O$ cryogel emphasized the ~63 nm scale. We attribute these to characteristic periodicities of consolidated domains and/or inter-domain spacings that emerge during drying-induced coalescence. The shift toward larger characteristic length (~63 nm) in $H_2O$ cryogels is consistent with ice templating and extensive matrix reorganization during freezing, whereas supercritical drying preserves smaller length scales formed during antisolvent demixing. The ambient-dried xerogel beads show a certain level of anisotropy, whereas the other beads are generally isotropic. Note the shift of the inflection point in the slopes from shorter to longer dimension when going from aerogel, to tBuOH-cryogel, to cryogel. This indicates an increase in the dimension of some characteristic scattering feature, when the beads are dried using a drying method causing increased consolidation of the cellulose matrix.

These trends align with prior SAXS observations in cellulose systems. During regeneration from [DBNH][OAc], in situ SAXS has revealed growth of low-q intensity and ~tens-of-nanometers density fluctuations consistent with spinodal-like demixing, whereas NMMO·$H_2O$ dopes show distinct behavior and early crystalline ordering without draw (Nishiyama et al. 2019). Nishiyama et al. observed marked low-q intensity increases and emergence of ~40 nm density fluctuations during regeneration from [DBNH][OAc], consistent with spinodal-like phase separation. In [TMGH][OAc]-derived aerogels, nanofibrillar radii ($R_g \approx 2.5$-3.0 nm) are preserved (Plappert et al. 2018), supporting the view that benign drying routes maintain fine features. Our aerogel data similarly show elevated low-q intensity with intermediate PE values, while the $H_2O$ cryogel and xerogel approach $q^{-4}$ behavior as interfaces smooth under consolidation.

The special value of Figure 6 is the direct, side-by-side comparison of SAXS across identical precursor hydrogels subjected to four drying routes in an SBIL/OES system. By quantifying both Porod regimes and characteristic length scales (~30 and ~63 nm), these data connect macroscopic drying histories to nanoscale interfacial morphology, complementing SEM and gas sorption and providing a basis for choosing drying conditions to target specific mesostructures.

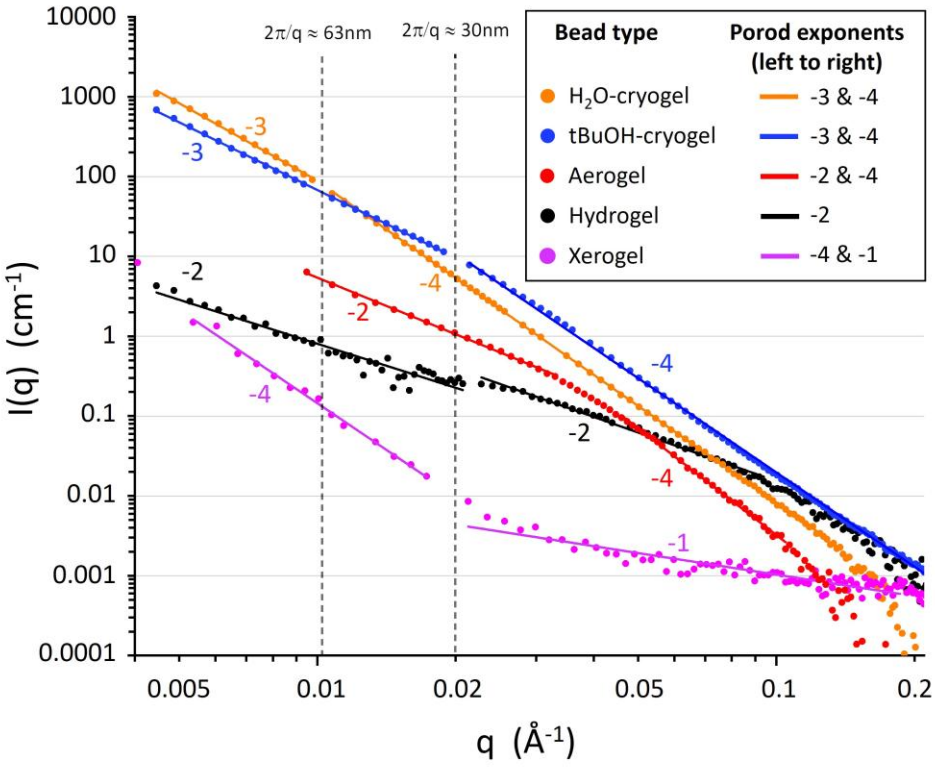



**Fig. 6** Small angle X-ray scattering (SAXS) diffractogram of the different types of beads: hydrogel, aerogel, tBuOH-cryogel, $H_2O$-cryogel and xerogel beads. Solid lines show linear fits in log-log representation, yielding Porod exponents (PE) from $I(q) \sim q^{(-PE)}$; rounded -PE values are indicated. The two vertical dashed lines mark $q \approx 0.010$ and 0.021 $Å^{-1}$, corresponding to real-space length scales $d \approx 63$ and 30 nm ($d = 2\pi/q$), where changes in slope appear. Aerogel and tBuOH cryogel emphasize ~30 nm features, whereas $H_2O$ cryogel emphasizes ~63 nm, consistent with increased consolidation and ice-templated reorganization. Xerogel exhibits reduced low-q intensity and extended $q^{-4}$ behavior, in agreement with its dense, near non-porous structure.

## Compression testing, DMA

Deformation of a porous cellular polymer network under compressive stress can usually be divided into three types: elastic bending, elastic buckling and plastic collapse. (Gibson & Ashby 1982) At low strain values stress-strain correlation is linear and the material compresses elastically, which is represented by the materials Young's modulus. Initially the cell walls buckle elastically but under increasing strain the deformation inevitably turns plastic. At intermediate strain values the yield point is reached, after which the linear behaviour ends and buckling of cell walls takes over. This portion of the curve following the yield point is often called the stress plateau, where very minor increases in stress lead to major increases in strain. Finally at high strain values opposite walls of collapsed pores start to touch and wall material starts to compress: the stress plateau transforming into a steepening stress-strain curve. Resilience is a term used to describe the ability of a material to absorb and release applied energy elastically, pertaining to the applied stress and induced strain before the yield point. Toughness is also a term used to describe a materials ability to absorb and release applied energy, but in contrast to resilience, it encompasses the plastic deformation and therefore is a measure of a materials total ability to absorb energy via deformation. However, in some cases no appreciable yield point can be detected, implying that the material does not exhibit elastic deformation.

While the above-mentioned scenario describes the ideal case, correspondingly similar behaviour are also observed in practise during compression testing of cellulose materials. For example when aerogels, derived from antisolvent regenerated dopes of cotton linters dissolved in either TBAF/DMSO or Ca(SCN)2·8$H_2O$/LiCl, were subjected to compression testing, an initial elastic bending at low values of compressive stress was observed. (Pircher et al. 2016) This was followed by a notable plateau region in the stress/strain curve (increased strain under very little additional stress) originating from elastic cell buckling in a range from 15 to 40 % strain. Eventually the plateau steepened when plastic collapse became dominant. On the other hand, similar aerogels from NMMO·$H_2O$ or [emim][OAc] dopes showed very little or no sign of cell buckling, transitioning gently from elastic bending to plastic collapse over a wide range in stress. The specific modulus of the samples ranged from 76 MPa $cm^3$ $g^{-1}$ for TBAF/DMSO (3 wt-% cellulose) to 68 MPa $cm^3$ $g^{-1}$ for NMMO·$H_2O$ (3 wt-%) and $Ca(SCN)_2$·8$H_2O$/LiCl (2 wt-%) to 20 MPa $cm^3$ $g^{-1}$ for [emim][OAc], with the TBAF/DMSO sample being notably rigid and brittle and the [emim][OAc] sample being very ductile.

The density of a cellulose matrix has a straightforward positive correlation with the degree of resilience expressed by the materials, such as NFC foams and aerogels. (Sehaqui et al. 2010, Sehaqui et al. 2011) An increase in density from 7 mg/$cm^3$ to 103 mg/$cm^3$ (foam) and from 14 mg/$cm^3$ to 105 mg/$cm^3$ (aerogel) yielded a significant increase in Young's modulus (56 kPa to 5310 kPa for foam, 35 kPa to 2800 kPa for aerogel) and yield stress (8 kPa to 516 kPa for foam, 3 kPa to 238 kPa for aerogel) under compressive testing. A similar relationship was observed in aerogels derived from [emim][OAc]-cellulose dope regenerated in $H_2O$ (Sescousse et al. 2011) and [TMGH][OAc]-cellulose dope regenerated in EtOH (Plappert et al. 2018), where under uniaxial compression the Young's modulus (E), density-normalized specific modulus and plateau stress of the aerogels were shown to increase significantly with density. (Plappert et al. 2018) The [TMGH][OAc]-dope derived aerogels were able to deform elastically up to a yield point of between 6.8 % to 12.3 % strain (in-solution cellulose concentrations of 5 wt-% and 1 wt-% and densities of 80 mg/$cm^3$ and 15 mg/$cm^3$ respectively) and a maximum in resilience was reached at 13.44 mJ/$cm^3$, corresponding to 206.7 mJ/g in the 4 wt-% 65 mg/$cm^3$ aerogel. Furthermore, no buckling or change in the diameter of the sample cylinder under compressive strain was observed in the [emim][OAc]-dope derived aerogels, demonstrating that the aerogels Poisson's ratio was zero. This is perhaps not surprising as many low-density cellulose II aerogels are irreversibly compressible without breakage up to 80 % strain, which usually marks the final upturn in the stress-strain curve. (Budtova 2019)

The response of the various cellulose beads to uniaxial compression was measured on a universal testing machine up to a load of 60 N. All the measurements were done in triplicate and as such the solid lines represent an average polynomial fit for three beads of each type, individual measurement points shown as light-coloured dots (Figure 7). The xerogel beads differ considerably in their toughness in comparison to the other bead types. As can be seen from Figure 7, a compressive stress of ca. 1000 kPa is recuired to achieve 50 % strain for the two cryogel and hydrogel beads, whereas a stress of 80 000 kPa is required to achieve similar strain in the xerogel beads. The two different cryogel and the hydrogel have a largely identical response to compression: very low resilience or toughness below 60 % strain and a steepening response to stress only at high strain values (> 85 %), at which point the beads have already been compacted to a very high degree. Hence, the stress response in these cryogel and hydrogel beads most likely arises from compression of the cell wall material itself when the majority of pores have totally collapsed, and the cell walls start to touch each other. The xerogel beads differ from all the other samples in their initial resistance to deformation, with ca. 20 000 kPa required to achieve a 10 % strain. Between 10 and 20 % strain a knee can be observed in the stress-strain curve, which is most likely a result of cracking of the beads due to increasing stress. The knee likely indicates crack initiation, which is consistent with dense xerogel microstructure. The fact that it takes place at exactly the same value for all the three individual xerogel beads rules out the possibility of a fluke material defect such as an air bubble.

The yield strength of nanocelluloses has been shown to be highly dependent on the moisture content, where small amounts of $H_2O$ provide beneficial effects on the interfacial strength,(Hou et al. 2021) but further increases to moisture content leads to decreases in both modulus and yield strength.(Sinko & Keten 2014, Yang et al. 2021) The small molecule mobile $H_2O$ helps in countering the imperfect fitting between two cellulose crystal lattices by providing broader and more comprehensive contact between the cellulose fibrils, but at higher quantities the growing $H_2O$ layer lubricating the cellulose interfibril surfaces reduces friction and prevents proper load transfer between the two.(Hou et al. 2021) The moisture content of the various dry beads in these measurements is estimated at ca. 5 wt-%, whereas the moisture content of the hydrogel is in large excess at 92 wt-%. (Leskinen et al. 2024b)

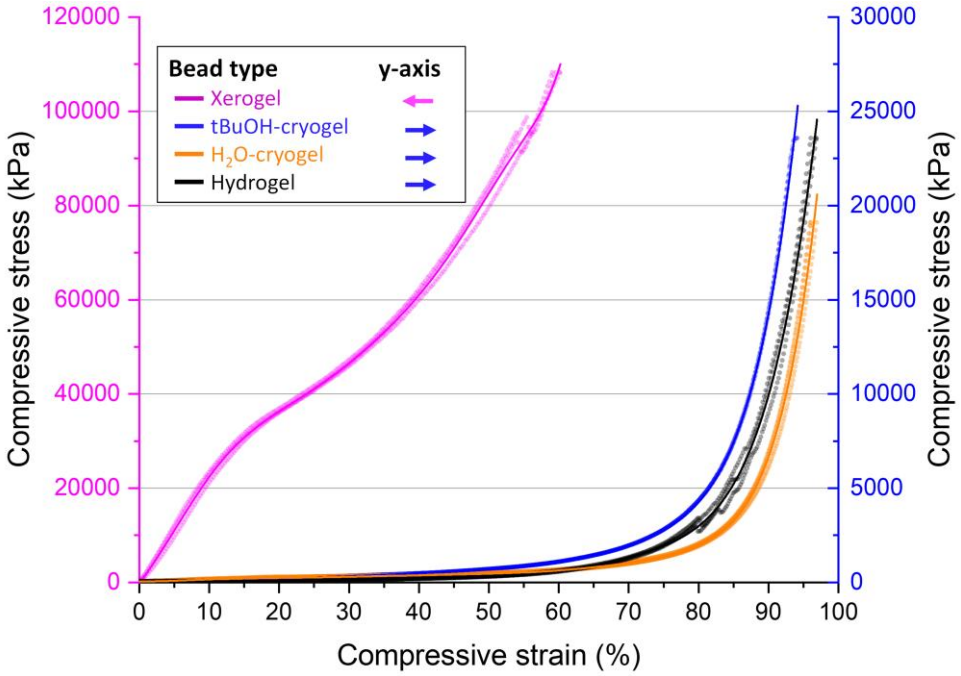



**Fig. 7** Percentile deformation (strain) of the different cellulose beads under compressive stress. Each stress/strain polynomial curve fit is composed of the average of three beads, each compressed individually. The compressive stress experienced by the xerogel material is presented on the left y-axis (pink), while that experienced by the other bead materials is presented on the right y-axis (blue).

# Conclusions

This work demonstrates, for the first time, a systematic comparison of four drying routes applied to identical cellulose beads regenerated from a [DBNH][OAc]/DMSO organic electrolyte solution into water. We show that drying controls mesoporosity and interfacial morphology of the cellulose beads starting from identical hydrogels, ambient drying, freeze-drying from $H_2O$ or tBuOH, and supercritical $CO_2$ drying yielded xerogels, cryogels, and aerogels with markedly different porosities and interfacial morphologies. Aerogels exhibited high mesoporosity (SSA 450 $m^2\ g^{-1}$, mesopore volume 1.98 $cm^3\ g^{-1}$), tBuOH cryogels showed intermediate porosity (123 $m^2\ g^{-1}$, 0.45 $cm^3\ g^{-1}$), and $H_2O$ cryogels were less porous (29 $m^2\ g^{-1}$, 0.06 $cm^3\ g^{-1}$), whereas xerogels were essentially non-porous (0.04 $m^2\ g^{-1}$) and visually transparent. SEM revealed regeneration-derived spherical 0.5-0.7 µm substructures in aerogels that progressively consolidated in cryogels and disappeared in xerogels. SAXS identified characteristic length scales near ~30 and ~63 nm and Porod regimes that transitioned from rougher interfaces (aerogels, PE ≈ 3.5-3.8) to smoother, near-Porod interfaces ($H_2O$ cryogels/xerogels, PE ≈ 3.9-4.0), directly linking drying severity to nanoscale consolidation. These findings confirm our hypothesis that drying routes minimizing capillary forces and ice templating best preserve regeneration-formed mesostructure in SBIL/OES-derived cellulose. The combined SEM-BET-SAXS evidence provides actionable and practical guidance for selecting drying protocols to tailor pore architecture for adsorption and related applications. Future work should employ in situ SAXS during drying to track dynamic evolution of the ~10-100 nm features and explore how dope concentration and antisolvent exchange kinetics modulate the preserved length scales.

## Acknowledgments

Cross-sectioning of beads for SEM was performed by Antti Salminen and Mervi Lindman from Electron Microscopy Unit (EMBI), Institute of Biotechnology, University of Helsinki, Finland.

The facilities of the ALD Center Finland, University of Helsinki, research infrastructure were used for SEM imaging.

The authors gratefully acknowledge Dr. Marco Beaumont at Aalto University, Finland, on their contribution on the $N_2$ sorption and Compression measurements, and discussions during the conception of the article.

The authors gratefully acknowledge Dr. Sabine Rosenfeldt at University of Bayreuth, Germany, for their technical assistance and expertise in conducting the SAXS measurements.

## Author contributions

Matti Leskinen: Conceptualization, Methodology, Investigation, Writing original draft, Writing - review and editing. Marianna Kemell: Investigation - SEM. Ilkka Kilpeläinen: Writing - review and editing. Vladimir Aseyev: Conceptualization, Writing - review and editing, Supervision. All authors read and approved of the final manuscript.

## Funding

This research was financially supported by the Research Council of Finland (grant no. 310481) and by the Alfred Kordelin Foundation (grant no. 220191, scholarship for M. Leskinen). Open access funding was provided by the University of Helsinki.

## Data availability

The raw and processed data required to reproduce these findings will be shared on request.

# Declarations

## Ethics approval and consent to participate

The article manuscript has not been submitted to multiple publications for simultaneous consideration. The submitted research is original and has not been published elsewhere in any form or language (in part or in whole). No potential conflicts of interest existed between researchers, and informed consent was obtained from all individual participants included in the study.

## Human and animal rights

We declare that no experiments on animal or human participants were conducted in the study.

## Consent for publication

The participants have agreed to submit the article manuscript to the journal.

## Competing interests

The authors have no competing interests to declare that are relevant to the content of this article.

# References

Aaltonen O, Jauhiainen O (2009) The preparation of lignocellulosic aerogels from ionic liquid solutions. Carbohydr Polym 75:125–129. https://doi.org/10.1016/j.carbpol.2008.07.008

Allen H, Wei D, Gu Y, Li S (2021) A historical perspective on the regulation of cellulose biosynthesis. Carbohydrate Polymers 252:117022. https://doi.org/10.1016/j.carbpol.2020.117022

Bai Y-X, Li Y-F (2006) Preparation and characterization of crosslinked porous cellulose beads. Carbohydrate Polymers 64:402–407. https://doi.org/10.1016/j.carbpol.2005.12.009

Beaumont M, Kondor A, Plappert S, et al (2017) Surface properties and porosity of highly porous, nanostructured cellulose II particles. Cellulose 24:435–440. https://doi.org/10.1007/s10570-016-1091-y

Beaumont M, Rennhofer H, Opietnik M, et al (2016) Nanostructured Cellulose II Gel Consisting of Spherical Particles. ACS Sustain Chem Eng 4:4424–4432. https://doi.org/10.1021/acssuschemeng.6b01036

Biganska O, Navard P (2005) Kinetics of Precipitation of Cellulose from Cellulose−NMMO−Water Solutions. Biomacromolecules 6:1948–1953. https://doi.org/10.1021/bm040079q

Biganska O, Navard P (2009) Morphology of cellulose objects regenerated from cellulose–N-methylmorpholine N-oxide–water solutions. Cellulose 16:179–188. https://doi.org/10.1007/s10570-008-9256-y

Biganska O, Navard P, Bédué O (2002) Crystallisation of cellulose/N-methylmorpholine-N-oxide hydrate solutions. Polymer 43:6139–6145. https://doi.org/10.1016/S0032-3861(02)00552-9

Buchtová N, Budtova T (2016) Cellulose aero-, cryo- and xerogels: towards understanding of morphology control. Cellulose 23:2585–2595. https://doi.org/10.1007/s10570-016-0960-8

Budtova T (2019) Cellulose II aerogels: a review. Cellulose 26:81–121. https://doi.org/10.1007/s10570-018-2189-1

Cai J, Kimura S, Wada M, et al (2008) Cellulose Aerogels from Aqueous Alkali Hydroxide–Urea Solution. ChemSusChem 1:149–154. https://doi.org/10.1002/cssc.200700039

Carrick C, Pendergraph SA, Wågberg L (2014) Nanometer Smooth, Macroscopic Spherical Cellulose Probes for Contact Adhesion Measurements. ACS Appl Mater Interfaces 6:20928–20935. https://doi.org/10.1021/am505673u

Carrick C, Ruda M, Pettersson B, et al (2013) Hollow cellulose capsules from CO2 saturated cellulose solutions—their preparation and characterization. RSC Adv 3:2462. https://doi.org/10.1039/c2ra22020b

Clough MT (2017) Organic electrolyte solutions as versatile media for the dissolution and regeneration of cellulose. Green Chem 19:4754–4768. https://doi.org/10.1039/C7GC01776F

Demilecamps A, Reichenauer G, Rigacci A, Budtova T (2014) Cellulose–silica composite aerogels from “one-pot” synthesis. Cellulose 21:2625–2636. https://doi.org/10.1007/s10570-014-0314-3

Deng M, Zhou Q, Du A, et al (2009) Preparation of nanoporous cellulose foams from cellulose-ionic liquid solutions. Mater Lett 63:1851–1854. https://doi.org/10.1016/j.matlet.2009.05.064

Ding M, Yu J, He J, Zhang J (2015) An unusual spherulite morphology induced by nano-fillers from a concentrated cellulose/ionic liquid solution. RSC Adv 5:44648–44651. https://doi.org/10.1039/C5RA06740E

Druel L, Niemeyer P, Milow B, Budtova T (2018) Rheology of cellulose-[DBNH][$CO_2$Et] solutions and shaping into aerogel beads. Green Chem 20:3993–4002. https://doi.org/10.1039/C8GC01189C

834 Fernandes AN, Thomas LH, Altaner CM, et al (2011) Nanostructure of cellulose microfibrils in
835 spruce wood. Proceedings of the National Academy of Sciences 108:.
836 https://doi.org/10.1073/pnas.1108942108
837 Ganesan K, Dennstedt A, Barowski A, Ratke L (2016) Design of aerogels, cryogels and xerogels of
838 cellulose with hierarchical porous structures. Mater Des 92:345–355.
839 https://doi.org/10.1016/j.matdes.2015.12.041
840 Gavillon R, Budtova T (2008) Aerocellulose: New Highly Porous Cellulose Prepared from
841 Cellulose−NaOH Aqueous Solutions. Biomacromolecules 9:269–277.
842 https://doi.org/10.1021/bm700972k
843 Gericke M, Liebert T, Seoud OAE, Heinze T (2011) Tailored Media for Homogeneous Cellulose
844 Chemistry: Ionic Liquid/Co-Solvent Mixtures. Macromol Mater Eng 296:483–493.
845 https://doi.org/10.1002/mame.201000330
846 Gibson LJ, Ashby MF (1982) The Mechanics of Three-Dimensional Cellular Materials. Proceedings
847 of the Royal Society of London Series A, Mathematical and Physical Sciences 382:43–59
848 Gupta S, Martoïa F, Orgéas L, Dumont PJJ (2018) Ice-Templated Porous Nanocellulose-Based
849 Materials: Current Progress and Opportunities for Materials Engineering. Applied Sciences 8:2463.
850 https://doi.org/10.3390/app8122463
851 Hauru LKJ, Hummel M, Nieminen K, et al (2016) Cellulose regeneration and spinnability from
852 ionic liquids. Soft Matter 12:1487–1495. https://doi.org/10.1039/C5SM02618K
853 Holding AJ (2016) Ionic Liquids and Electrolytes for Cellulose Dissolution. Dissertation, University
854 of Helsinki. https://doi.org/10.13140/RG.2.2.21504.23045
855 Hou Y, Guan Q-F, Xia J, et al (2021) Strengthening and Toughening Hierarchical Nanocellulose via
856 Humidity-Mediated Interface. ACS Nano 15:1310–1320. https://doi.org/10.1021/acsnano.0c08574
857 Ilyin SO, Makarova VV, Anokhina TS, et al (2018) Diffusion and phase separation at the
858 morphology formation of cellulose membranes by regeneration from N-methylmorpholine N-oxide
859 solutions. Cellulose 25:2515–2530. https://doi.org/10.1007/s10570-018-1756-9
860 Imagawa K, Omura T, Ihara Y, et al (2017) Preparation of disk-like cellulose particles. Cellulose
861 24:3111–3118. https://doi.org/10.1007/s10570-017-1342-6
862 Ishida O, Kim D-Y, Kuga S, et al (2004) Microfibrillar carbon from native cellulose. Cellulose
863 11:475–480. https://doi.org/10.1023/B:CELL.0000046410.31007.0b
864 Isobe N, Kimura S, Wada M, Kuga S (2012) Mechanism of cellulose gelation from aqueous alkali-
865 urea solution. Carbohydr Polym 89:1298–1300. https://doi.org/10.1016/j.carbpol.2012.03.023
866 Jin H, Nishiyama Y, Wada M, Kuga S (2004) Nanofibrillar cellulose aerogels. Colloids Surf A:
867 Physicochem Eng Asp 240:63–67. https://doi.org/10.1016/j.colsurfa.2004.03.007
868 Johns MA, Bernardes A, De Azevêdo ER, et al (2017) On the subtle tuneability of cellulose
869 hydrogels: implications for binding of biomolecules demonstrated for CBM 1. J Mater Chem B
870 5:3879–3887. https://doi.org/10.1039/C7TB00176B
871 Kasraian K, DeLuca PP (1995) Thermal Analysis of the Tertiary Butyl Alcohol-Water System and
872 Its Implications on Freeze-Drying. Pharm Res 12:484–490.
873 https://doi.org/10.1023/A:1016233408831

King AWT, Asikkala J, Mutikainen I, et al (2011) Distillable Acid–Base Conjugate Ionic Liquids for Cellulose Dissolution and Processing. Angew Chem Int Ed 50:6301–6305. https://doi.org/10.1002/anie.201100274

Kobayashi Y, Saito T, Isogai A (2014) Aerogels with 3D Ordered Nanofibre Skeletons of Liquid-Crystalline Nanocellulose Derivatives as Tough and Transparent Insulators. Angew Chem Int Ed 53:10394–10397. https://doi.org/10.1002/anie.201405123

Kuzmina O, Bhardwaj J, Vincent SR, et al (2017) Superbase ionic liquids for effective cellulose processing from dissolution to carbonisation. Green Chem 19:5949–5957. https://doi.org/10.1039/C7GC02671D

Leskinen M, Kilpeläinen I, Hietala S (2024a) Interaction of cellulose and water upon drying and swelling by 13C CP/MAS NMR. Cellulose 31:10745–10769. https://doi.org/10.1007/s10570-024-06227-7

Leskinen M, Mirzaei Z, Kemell M, et al (2024b) Formation of core–shell structures and viscous fingering in cellulose beads regenerated from [DBNH][OAc]/DMSO. Cellulose 31:10253–10269. https://doi.org/10.1007/s10570-024-06217-9

Li H, Kruteva M, Mystek K, et al (2020) Macro- and Microstructural Evolution during Drying of Regenerated Cellulose Beads. ACS Nano 14:6774–6784. https://doi.org/10.1021/acsnano.0c00171

Liao Y, Pang Z, Pan X (2019) Fabrication and Mechanistic Study of Aerogels Directly from Whole Biomass. ACS Sustain Chem Eng 7:17723–17736. https://doi.org/10.1021/acssuschemeng.9b04032

Liebner F, Potthast A, Rosenau T, et al (2008) Cellulose aerogels: Highly porous, ultra-lightweight materials. Holzforschung 62:129–135. https://doi.org/10.1515/HF.2008.051

Lin F, You Y, Yang X, et al (2017) Microwave-assisted facile synthesis of TEMPO-oxidized cellulose beads with high adsorption capacity for organic dyes. Cellulose 24:5025–5040. https://doi.org/10.1007/s10570-017-1473-9

Lin W-H, Jana SC (2021) Analysis of porous structures of cellulose aerogel monoliths and microparticles. Microporous Mesoporous Mater 310:110625. https://doi.org/10.1016/j.micromeso.2020.110625

Lu A, Liu Y, Zhang L, Potthast A (2011) Investigation on Metastable Solution of Cellulose Dissolved in NaOH/Urea Aqueous System at Low Temperature. J Phys Chem B 115:12801–12808. https://doi.org/10.1021/jp206643f

Luo X, Zhang L (2009) High effective adsorption of organic dyes on magnetic cellulose beads entrapping activated carbon. J Hazard Mater 171:340–347. https://doi.org/10.1016/j.jhazmat.2009.06.009

Luo X, Zhang L (2010) Immobilization of Penicillin G Acylase in Epoxy-Activated Magnetic Cellulose Microspheres for Improvement of Biocatalytic Stability and Activities. Biomacromolecules 11:2896–2903. https://doi.org/10.1021/bm100642y

Mi Q, Ma S, Yu J, et al (2016) Flexible and Transparent Cellulose Aerogels with Uniform Nanoporous Structure by a Controlled Regeneration Process. ACS Sustainable Chem Eng 4:656–660. https://doi.org/10.1021/acssuschemeng.5b01079

Moser C, Henriksson G, Lindström ME (2016) Specific surface area increase during cellulose nanofibre manufacturing related to energy input. BioResources 11:7124–7132

915 Motozato Y, Hirayama C (1984) Preparation and properties of cellulose spherical particles and their
916 ion exchangers. J Chromatogr A 298:499–507. https://doi.org/10.1016/S0021-9673(01)92747-5
917 Nemoto J, Saito T, Isogai A (2015) Simple Freeze-Drying Procedure for Producing Nanocellulose
918 Aerogel-Containing, High-Performance Air Filters. ACS Appl Mater Interfaces 7:19809–19815.
919 https://doi.org/10.1021/acsami.5b05841
920 Niimura H, Yokoyama T, Kimura S, et al (2010) AFM observation of ultrathin microfibrils in fruit
921 tissues. Cellulose 17:13–18. https://doi.org/10.1007/s10570-009-9361-6
922 Nishiyama Y, Asaadi S, Ahvenainen P, Sixta H (2019) Water-induced crystallization and nano-scale
923 spinodal decomposition of cellulose in NMMO and ionic liquid dope. Cellulose 26:281–289.
924 https://doi.org/10.1007/s10570-018-2148-x
925 Omura T, Imagawa K, Kono K, et al (2017) Encapsulation of Either Hydrophilic or Hydrophobic
926 Substances in Spongy Cellulose Particles. ACS Appl Mater Interfaces 9:944–949.
927 https://doi.org/10.1021/acsami.6b13261
928 Paajanen A, Ceccherini S, Maloney T, Ketoja JA (2019) Chirality and bound water in the
929 hierarchical cellulose structure. Cellulose 26:5877–5892. https://doi.org/10.1007/s10570-019-
930 02525-7
931 Park S, Baker JO, Himmel ME, et al (2010) Cellulose crystallinity index: measurement techniques
932 and their impact on interpreting cellulase performance. Biotechnology for Biofuels 3:10.
933 https://doi.org/10.1186/1754-6834-3-10
934 Parviainen A, King AWT, Mutikainen I, et al (2013) Predicting Cellulose Solvating Capabilities of
935 Acid–Base Conjugate Ionic Liquids. ChemSusChem 6:2161–2169.
936 https://doi.org/10.1002/cssc.201300143
937 Pircher N, Carbajal L, Schimper C, et al (2016) Impact of selected solvent systems on the pore and
938 solid structure of cellulose aerogels. Cellulose 23:1949–1966. https://doi.org/10.1007/s10570-016-
939 0896-z
940 Plappert SF, Nedelec J-M, Rennhofer H, et al (2018) Self-Assembly of Cellulose in Super-Cooled
941 Ionic Liquid under the Impact of Decelerated Antisolvent Infusion: An Approach toward
942 Anisotropic Gels and Aerogels. Biomacromolecules 19:4411–4422.
943 https://doi.org/10.1021/acs.biomac.8b01278
944 Qiao L, Li S, Du K (2020) Fabrication and characterization of porous cellulose beads with high
945 strength and specific surface area via preliminary chemical cross-linking reaction for protein
946 separation. Biochem Eng J 153:107412. https://doi.org/10.1016/j.bej.2019.107412
947 Rajeev A, Basavaraj MG (2019) Confinement effect on spatio-temporal growth of spherulites from
948 cellulose/ionic liquid solutions. Polymer 185:121927.
949 https://doi.org/10.1016/j.polymer.2019.121927
950 Robitzer M, Renzo FD, Quignard F (2011) Natural materials with high surface area. Physisorption
951 methods for the characterization of the texture and surface of polysaccharide aerogels. Microporous
952 Mesoporous Mater 140:9–16. https://doi.org/10.1016/j.micromeso.2010.10.006
953 Roy C, Budtova T, Navard P (2003) Rheological Properties and Gelation of Aqueous
954 Cellulose−NaOH Solutions. Biomacromolecules 4:259–264. https://doi.org/10.1021/bm020100s

Saito T, Uematsu T, Kimura S, et al (2011) Self-aligned integration of native cellulose nanofibrils towards producing diverse bulk materials. Soft Matter 7:8804. https://doi.org/10.1039/c1sm06050c

Sandig B, Michalek L, Vlahovic S, et al (2015) A Monolithic Hybrid Cellulose-2.5-Acetate/Polymer Bioreactor for Biocatalysis under Continuous Liquid–Liquid Conditions Using a Supported Ionic Liquid Phase. Chemistry A European J 21:15835–15842. https://doi.org/10.1002/chem.201501618

Schaaf P, Lotz B, Wittmann JC (1987) Liquid-liquid phase separation and crystallization in binary polymer systems. Polymer 28:193–200. https://doi.org/10.1016/0032-3861(87)90403-4

Sehaqui H, Salajková M, Zhou Q, Berglund LA (2010) Mechanical performance tailoring of tough ultra-high porosity foams prepared from cellulose I nanofibre suspensions. Soft Matter 6:1824. https://doi.org/10.1039/b927505c

Sehaqui H, Zhou Q, Berglund LA (2011) High-porosity aerogels of high specific surface area prepared from nanofibrillated cellulose (NFC). Compos Sci Technol 71:1593–1599. https://doi.org/10.1016/j.compscitech.2011.07.003

Sescousse R, Gavillon R, Budtova T (2011) Aerocellulose from cellulose–ionic liquid solutions: Preparation, properties and comparison with cellulose–NaOH and cellulose–NMMO routes. Carbohydr Polym 83:1766–1774. https://doi.org/10.1016/j.carbpol.2010.10.043

Sinko R, Keten S (2014) Effect of moisture on the traction-separation behavior of cellulose nanocrystal interfaces. Appl Phys Lett 105:243702. https://doi.org/10.1063/1.4904708

Sixta H, Michud A, Hauru L, et al (2015) Ioncell-F: A High-strength regenerated cellulose fibre. Nord Pulp Paper Res J 30:43–57. https://doi.org/10.3183/npprj-2015-30-01-p043-057

Song B, Zhao S, Shen W, et al (2020) Direct Measurement of Plant Cellulose Microfibril and Bundles in Native Cell Walls. Front Plant Sci 11:479. https://doi.org/10.3389/fpls.2020.00479

Song H, Niu Y, Yu J, et al (2013) Preparation and morphology of different types of cellulose spherulites from concentrated cellulose ionic liquid solutions. Soft Matter 9:3013. https://doi.org/10.1039/c3sm27320b

Stone JE, Scallan AM (1965) Effect of component removal upon the porous structure of the cell wall of wood. J Polym Sci, C Polym Symp 11:13–25. https://doi.org/10.1002/polc.5070110104

Sturm M, Helminen JKJ, Honkasalo A, et al (2023) Investigations for the use and recyclability of the ionic liquid [MTBDH][AcO] as a solvent in air-gap-wet spinning process. J Appl Polym Sci 140:e53901. https://doi.org/10.1002/app.53901

Suzuki T, Kono K, Shimomura K, Minami H (2014) Preparation of cellulose particles using an ionic liquid. J Colloid Interface Sci 418:126–131. https://doi.org/10.1016/j.jcis.2013.12.014

Swatloski RP, Spear SK, Holbrey JD, Rogers RD (2002) Dissolution of Cellose with Ionic Liquids. J Am Chem Soc 124:4974–4975. https://doi.org/10.1021/ja025790m

Thommes M, Kaneko K, Neimark AV, et al (2015) Physisorption of gases, with special reference to the evaluation of surface area and pore size distribution (IUPAC Technical Report). Pure Appl Chem 87:1051–1069. https://doi.org/10.1515/pac-2014-1117

Thygesen A, Oddershede J, Lilholt H, et al (2005) On the determination of crystallinity and cellulose content in plant fibres. Cellulose 12:563–576. https://doi.org/10.1007/s10570-005-9001-8

994 Trygg J, Fardim P, Gericke M, et al (2013) Physicochemical design of the morphology and
995 ultrastructure of cellulose beads. Carbohydr Polym 93:291–299.
996 https://doi.org/10.1016/j.carbpol.2012.03.085
997 van de Witte P, Dijkstra PJ, van den Berg JWA, Feijen J (1997) Metastable liquid-liquid and solid-
998 liquid phase boundaries in polymer-solvent-nonsolvent systems. J Polym Sci B Polym Phys 35:763–
999 770. https://doi.org/10.1002/(SICI)1099-0488(19970415)35:5%253C763::AID-
1000 POLB4%253E3.0.CO;2-N
1001 Yang X, Jungstedt E, Reid MS, Berglund LA (2021) Polymer Films from Cellulose Nanofibrils—
1002 Effects from Interfibrillar Interphase on Mechanical Behavior. Macromolecules 54:4443–4452.
1003 https://doi.org/10.1021/acs.macromol.1c00305
1004 Yildir E, Kolakovic R, Genina N, et al (2013) Tailored beads made of dissolved cellulose—
1005 Investigation of their drug release properties. Int J Pharm 456:417–423.
1006 https://doi.org/10.1016/j.ijpharm.2013.08.047
1007 Yu X, Kang D, Hu Y, et al (2014) One-pot synthesis of porous magnetic cellulose beads for the
1008 removal of metal ions. RSC Adv 4:31362. https://doi.org/10.1039/C4RA05601A
1009 Zaman A, Huang F, Jiang M, et al (2020) Preparation, Properties, and Applications of Natural
1010 Cellulosic Aerogels: A Review. Energy Built Environ 1:60–76.
1011 https://doi.org/10.1016/j.enbenv.2019.09.002
1012 Zeng B, Wang X, Byrne N (2020) Cellulose Beads Derived from Waste Textiles for Drug Delivery.
1013 Polymers 12:1621. https://doi.org/10.3390/polym12071621
1014 Zhao Z, Shklyaev OE, Nili A, et al (2013) Cellulose Microfibril Twist, Mechanics, and Implication
1015 for Cellulose Biosynthesis. J Phys Chem A 117:2580–2589. https://doi.org/10.1021/jp3089929
1016 Östlund Å, Idström A, Olsson C, et al (2013) Modification of crystallinity and pore size distribution
1017 in coagulated cellulose films. Cellulose 20:1657–1667. https://doi.org/10.1007/s10570-013-9982-7

## Supplementary Files

This is a list of supplementary files associated with this preprint. Click to download.

- GraphicalAbstract.jpg
- Scheme1.jpg